Development of Shape Memory Alloy Clamp by Wire Arc Additive Manufacturing for Temperature Based Self-Opening System

M.Tech. Thesis

By

HIMANSHU SEN

Roll No.: 2302103005

DEPARTMENT OF MECHANICAL ENGINEERING

INDIAN INSTITUTE OF TECHNOLOGY, INDORE

MAY 2024

Development of Shape Memory Alloy Clamp by Wire Arc Additive Manufacturing for Temperature Based Self-Opening System

A THESIS

Submitted in partial fulfillment of the requirements for the award of the degree

of

Master of Technology

by

HIMANSHU SEN

Roll No.: 2302103005

DEPARTMENT OF MECHANICAL ENGINEERING

INDIAN INSTITUTE OF TECHNOLOGY INDORE

MAY 2024

INDIAN INSTITUTE OF TECHNOLOGY, INDORE

CANDIDATE'S DECLARATION

I hereby certify that the work which is being presented in the thesis entitled "**Development of Shape Memory Alloy Clamp by Wire Arc Additive Manufacturing for Temperature Based Self-Opening System"** in the partial fulfillment of the requirements for the award of the degree of **MASTER OF TECHNOLOGY** and submitted in the **DEPARTMENT OF MECHANICAL ENGINEERING, Indian Institute of Technology Indore**, is an authentic record of my own work carried out during the time period from July, 2023 to May, 2025 under the supervision of Dr. I.A Palani, Professor, Department of Mechanical Engineering, Indian Institute of Technology, Indore and Dr. Suhas S. Joshi, Professor, Department of Mechanical Engineering, Indian Institute of Technology, Indore.

The matter presented in this thesis has not been submitted by me for the award of any other degree of this or any other institute.

Signature of the student
(Himanshu Sen)

This is to certify that the above statement made by the candidate is correct to the best of my/our knowledge.

Signature of the Supervisor of M.Tech. Thesis #1

(Prof. I.A Palani)

Signature of the Supervisor of M.Tech. Thesis #2

18.06.2025

(Prof. Suhas S Joshi)

Himanshu Sen has successfully given his MTech. Oral Examination held on **26/05/2025**.

Prof. I.A Palani
Date:18/06/2025

Prof. Suhas S Joshi
Date: 18.06.2025

Convener, DPGC
Date:19-06-2025

ACKNOWLEDGEMENTS

I extend my sincere gratitude to my supervisors, Prof. I.A. Palani and Prof. Suhas S. Joshi, from the Department of Mechanical Engineering, Indian Institute of Technology Indore, for their invaluable guidance and support throughout my M.Tech thesis. Their expertise and encouragement have been instrumental at every stage of my research. I am especially grateful to Prof. I.A. Palani for his unwavering support, motivation, and insightful guidance, which have greatly contributed to the success of this work.

I sincerely thank Prof. Suhas S. Joshi, Director of Indian Institute of Technology Indore, and my co-supervisor, for his esteemed supervision and invaluable guidance. His insights and support have been instrumental in shaping my research. I also wholeheartedly thank our HOD and course coordinator of MTech program. I would also like to express my gratitude to all faculty members, the DPGC convener, and PSPC members for their valuable technical discussions and constructive feedback, which have significantly enriched my M.Tech research work.

I want to thank all the members of Mechatronics and Instrumentation Lab., especially Dr. Anshu Sahu, Ms Diksha Jaurker, Mr. Kaushal Gangwar and Mr. Arpit Singh for their unwavering support, guidance and mentorship during my research work. Further, I would like to extend my gratitude to other group members and staff members from other laboratories, Sophisticated Instrumentation Centre, for the supportive environment.

I would like to express my heartfelt gratitude to my friends and family for their constant support.

Finally, I am grateful to God, my parents and sisters for their continuous encouragement and guidance.

DEDICATED TO RESEARCHERS IN ADDITIVE MANUFACTURING AND SMART MATERIALS

Abstract

Shape Memory alloys show a special property through which they can remember their parent shape, and this parent shape could be achieved from any other deformed shape by heating. In our study we are printing these shape memory alloys, i.e NiTi and $NiTiCu_x$ using a Wire Arc Additive Manufacturing (WAAM) setup. The deposition is cut into sheets using wire-Electric Discharge Machining and then trained for controlled actuation.

To achieve our objective, firstly the WAAM parameters are studied with respect to the uniformity and thickness of deposition. This is done by employing screening design and full factorial design for voltage, wire-feed rate and argon flow rate as input variables and thickness of deposition as output variable.

After completely understanding the WAAM operation, NiTi single layer deposition is done by using full factorial design and studied for uniformity and transformation temperature.

The optimal deposition is selected and tested for microstructure, composition, transformation temperature, tensile testing and micro-hardness testing. After analyzing the results, the need of heat treatment is found to be required. Hence, annealing of the optimized deposition is performed and compared to pristine sample for microstructure, composition, transformation temperature and mechanical properties.

Initial annealing yielded positive results. Subsequently, additional heat treatments, specifically solutionizing and aging, were performed to investigate their effect on the material's transformation temperature. Then, Cu inclusion is done in NiTi and their effect on transformation temperature along with other properties is studied.

After cutting the sheets from the above discussed depositions, the sheets are trained for shape setting.

The results show that successful training of the samples at required transformation temperature is done and hence our objective is achieved.

LIST OF PUBLICATIONS

- **Himanshu Sen**, Suhas S Joshi, I A Palani "An Investigation into Laser-hybrid Wire Arc Additive Manufacturing for Depositing Thin Sections of SS-304L" by COPEN-13 – Presented. (**Accepted for proceedings**)
- **Himanshu Sen**, Anshu Sahu, Suhas S Joshi, I A Palani "Thermo-mechanical and Microstructural Evaluation of Post-annealed Wire Arc Additive Manufactured (WAAM) Niti Alloys." is submitted for **IMECE-ASME - 2025** (**Under Review**)
- **Himanshu Sen**, Suhas S Joshi, I A Palani "Laser cleaning of Mild-steel" was presented at **National Laser Symposium**-33 (**Accepted for proceedings**)
- Anshu Sahu, KS Tomar, **Himanshu Sen**, I A Palani "Investigation on laser shock peening and laser nitriding of wire arc additive manufactured multilayer NiTi shape memory alloy" has been submitted for- **9th ICLPRP** (**Under Review**)

TABLE OF CONTENTS

LIST OF FIGURES

LIST OF TABLES

NOMENCLATURE

Symbol	Unit	Description
M_s	°C	Martensite start
M_f	°C	Martensite finish
A_s	°C	Austenite start
A_f	°C	Austenite finish

ACRONYMS

S.No.	Acronym	Expansion
1.	2D	Two-dimensional
2.	3D	Three-dimensional
3.	4D	Four-dimensional
4.	AM	Additive Manufacturing
5.	LASER	Light amplification by stimulated emission of radiation
6.	XRD	X-ray diffraction
7.	FE-SEM	Field emission scanning electron Microscope
8.	SMA	Shape Memory Alloys
9.	SME	Shape Memory Effect
10.	WAAM	Wire Arc Additive Manufacturing
11.	GMAW	Gas Metal Arc Welding

Chapter 1

Introduction

Shape memory alloys (SMAs) have emerged as a fascinating class of smart materials with unique properties that enable them to "remember" and return to their original shape after deformation. This comprehensive thesis background explores these remarkable materials, the promising Wire Arc Additive Manufacturing (WAAM) technology, and the specific NiTi and $NiTiCu_x$ alloy systems that demonstrate exceptional shape memory characteristics.

1.1 Historical Context

Nickel-titanium alloys, commercially known as Nitinol, are known for their unique shape memory effect (SME) and superelasticity. These properties arise from a reversible martensitic transformation between the high-temperature austenite and low-temperature martensite phases. The original discovery of SME in copper-based alloys in 1938, and subsequently in Au-Cd and other systems, set the stage for the development of Nitinol, which was patented in 1965 by Buger and Wang at the Naval Ordnance Laboratory. Nitinol's superior ductility and tensile strength have led to its adoption in aerospace, automotive, and especially biomedical fields, where it is used in stents, orthodontic wires, and various implants.

The advent of additive manufacturing, particularly 3D printing, has enabled the fabrication of complex Nitinol components, ushering in the era of 4D printing-where printed objects can change shape in response to external stimuli such as heat or stress. This innovation has expanded the design flexibility and functional integration of Nitinol-based devices, making AM a cost-effective and energy-efficient alternative to traditional manufacturing methods.[1]

1.1 Shape Memory Alloys and Their Properties

Shape Memory Alloys (SMAs) are a class of advanced functional materials characterized by two extraordinary properties: the shape memory effect (SME) and superelasticity (also known as pseudoelasticity). These unique attributes stem from the material's ability to undergo a reversible solid-state phase transformation between austenite and martensite phases[2], [3]

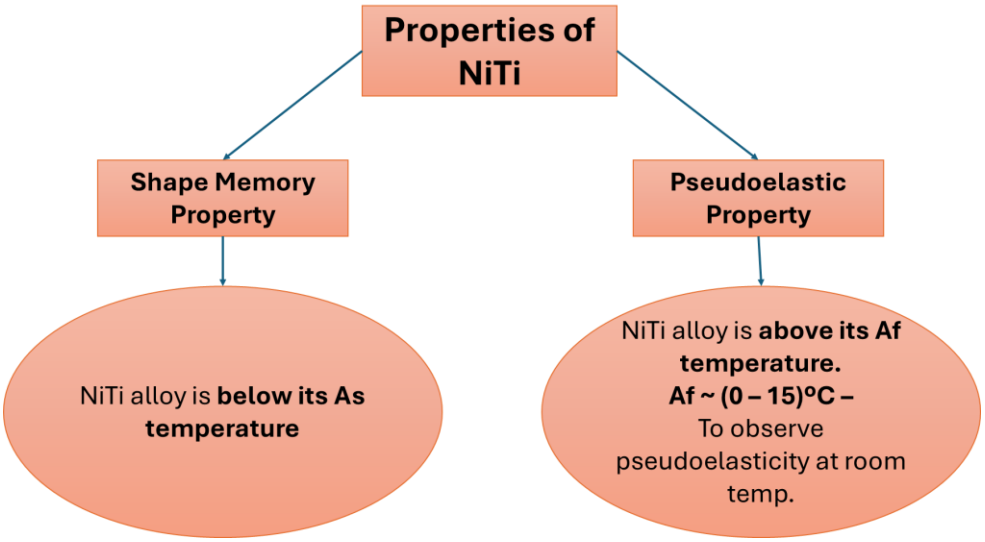

Fig 1.1 Properties of NiTi

The two main properties of NiTi are depicted in Figure 1. A NiTi alloy displays shape memory effect if it is in martensite phase at room temperature and it depicts pseudoelastic behavior if it is in austenite phase at room temperature. So, to utilize different properties of the NiTi alloy, we must control the transformation temperatures.

1.1.1 Fundamental Characteristics

The shape memory effect enables SMAs to recover their original shape after deformation when heated above a specific transition temperature. This occurs because the material can "remember" its pre-deformation shape through a thermo-mechanical process[3]. The material begins in its austenitic (parent) phase, transforms to martensite when cooled, and undergoes shape recovery when heated back to austenite[4]. This reversible transformation makes SMAs particularly valuable for applications requiring controlled actuation in response to temperature changes[2].

Superelasticity, in contrast, occurs at temperatures above the austenite finish temperature, allowing the material to undergo significant deformation (up to 8-10%) and then return to its original shape upon unloading, without requiring thermal activation[2], [3]. This property is fundamentally different from conventional elasticity as it involves a stress-induced martensitic transformation

rather than simple atomic bond stretching[5]. The shape memory property and pseudoelastic property are depicted below in Figure 2, Figure 3 and Figure 4

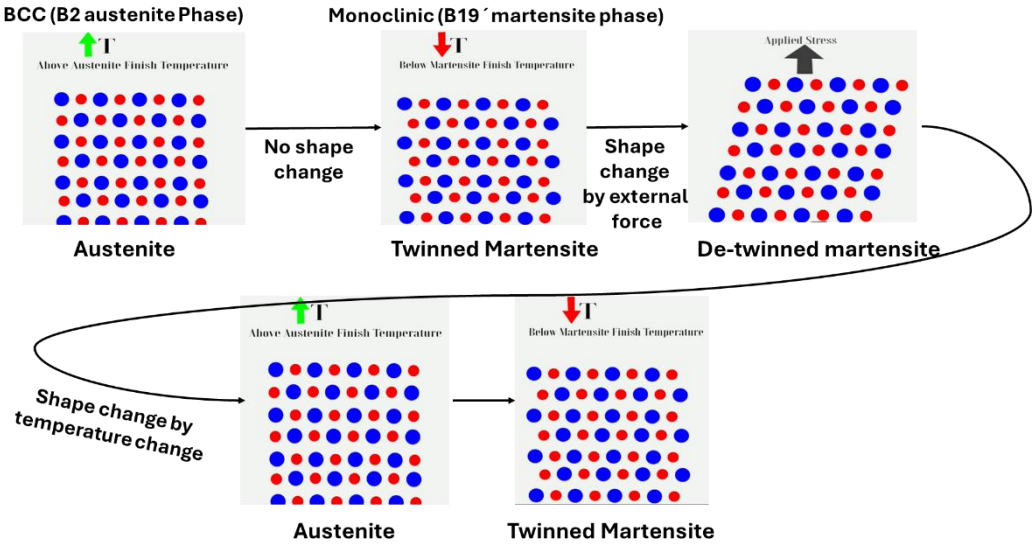

Fig. 1.2 Shape memory property of NiTi alloy

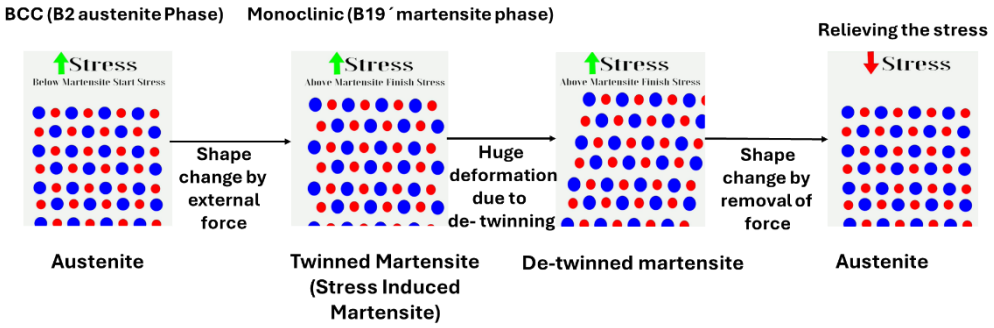

Fig. 1.3 Pseudoelastic property of NiTi alloy

1.1.2 Transformation Mechanisms

The shape memory mechanism in SMAs is directly associated with the martensitic transformation, which occurs through two primary mechanisms: self-accommodation and variant coalescence[4] .During cooling, the austenite phase transforms into multiple martensite variants that self-accommodate to minimize macroscopic shape change[4]. When external stress is applied, these variants reorient or coalesce, resulting in macroscopic shape change [4]. Upon heating, the martensite reverts to austenite, restoring the original shape[6]

The martensitic transformation in SMAs is characterized by four critical transformation temperatures: martensite start (Ms), martensite finish (Mf),

austenite start (As), and austenite finish (Af)[3]. These temperatures determine the operational range for both the shape memory effect and superelasticity, and can be tailored through alloy composition and thermomechanical processing [5], [6]

1.1.3 Mechanical Behavior and Material Properties

SMAs exhibit complex mechanical behavior, combining high specific strength, wear resistance, anti-fatigue characteristics, and high yield strength[2]. Their stress-strain behavior shows distinctive plateau regions during loading and unloading, representing the phase transformation zones[3]. This behavior enables SMAs to dissipate significant energy, making them valuable for damping and seismic applications[3].

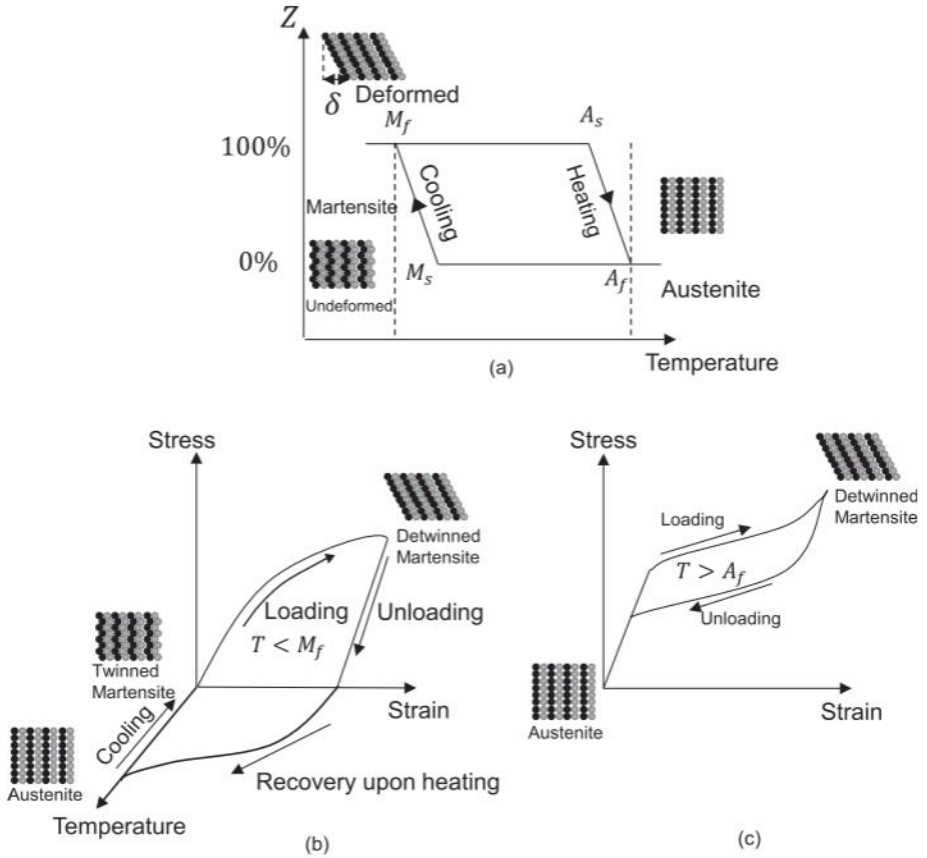

Fig. 1.4 Cyclic behaviour of SMAs (a)phase transformation between austenite and martensite (b) shape memory behaviour of SMAs, and (c)pseudoelastic behaviour of SMAs [3].

As depicted in Figure 4(a) and (b), when the temperature is below the austenite start temperature (As), a shape memory alloy (SMA) deforms under load and retains some strain after unloading. Upon heating above As, a phase transformation from martensite to austenite begins and completes at the austenite finish temperature (Af), restoring the original shape. This is known as the shape memory effect. SMA is fully martensitic below Mf and fully austenitic above Af [3].

Figure 4(c) illustrates the superelastic effect. When loaded beyond a certain stress, the SMA transforms into martensite, but upon unloading, it reverts to its original shape as the martensite becomes unstable. This property allows SMAs to recover deformation, making them valuable in structural applications under dynamic loads [3].

The mechanical properties of SMAs can be significantly affected by various factors including composition, thermomechanical processing, and cycling history[6]. Under cyclic loading, SMAs demonstrate a gradual evolution of transformation characteristics, often referred to as training, which stabilizes their properties for repeatable actuation[7]

1.2 Wire Arc Additive Manufacturing (WAAM)

Wire Arc Additive Manufacturing (WAAM) represents an innovative approach to metal fabrication that combines the principles of additive manufacturing with traditional arc welding technology. This process has gained significant attention for its potential to produce medium to large-sized components with complex geometries, high material efficiency, and relatively low equipment costs.[5]

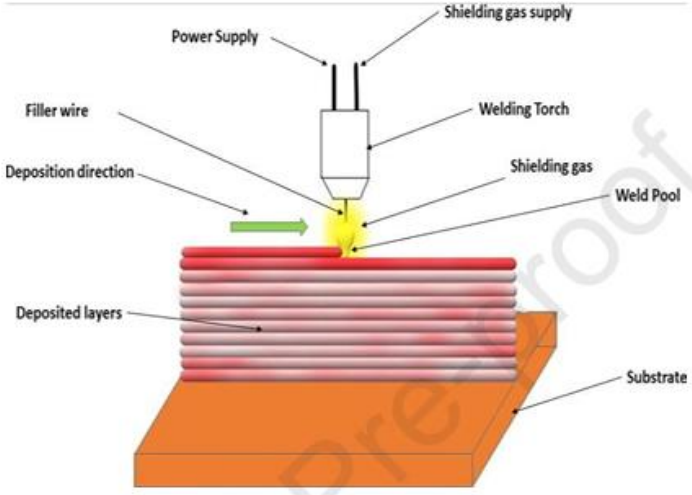

Fig. 1.5 Schematic diagram showing layers deposition in WAAM[8]

Figure 5 illustrates a standard WAAM setup. In this process, wire feedstock is melted using a suitable arc welding method, producing molten droplets that are deposited layer by layer on a substrate, gradually building up the final component. [8]

Additive Manufacturing (AM) is a method of creating components by adding layers of material, as opposed to the traditional subtractive manufacturing processes. Wire Arc Additive Manufacturing (WAAM) is a type of directed energy deposition process that utilizes an electric arc as the heat source and feeds wire through a nozzle [9]. AM process leads to a substantial decrease in the quantity of components needed for assembly. This reduction is a result of the intricate nature of the manufacturing techniques employed [10]. The process is known to significantly reduce the cost of building near-net-shape metal components with lesser production time [11].

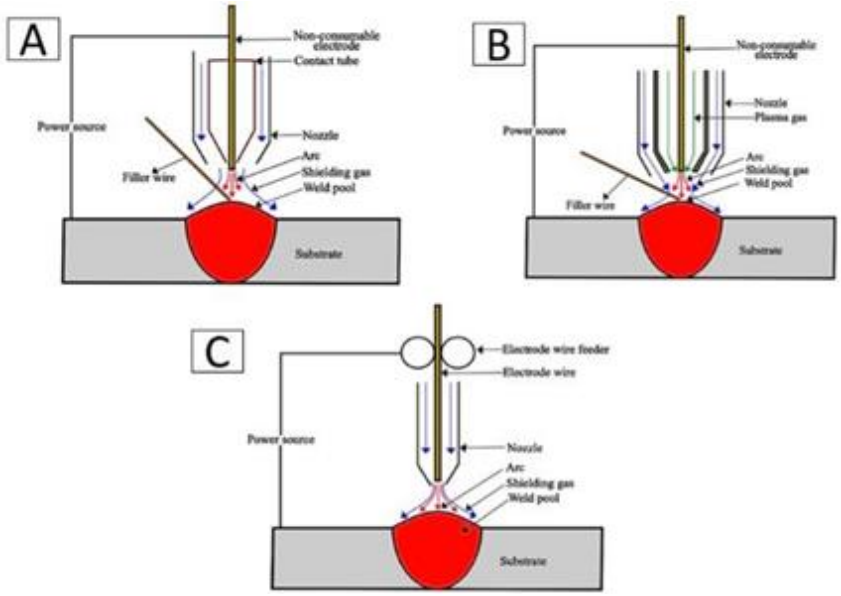

Fig. 1.6 Different Types of WAAM (A) GTAW, (B) PAW, (C) GMAW[8]

WAAM is categorized into three main arc-based methods: GTAW, PAW, and GMAW, as shown in Fig. 6 (A–C). GTAW uses a non-consumable tungsten electrode to melt filler wire, while PAW improves efficiency with a constricted arc. GMAW, the most common, uses a consumable wire and offers high deposition rates. It includes MIG for non-ferrous and MAG for ferrous metals. GMAW operates in four metal transfer modes, with Cold Metal Transfer (CMT) being a key advancement due to its low heat input and minimal spatter. WAAM is ideal for large metal components and repairs but faces challenges like residual stress and

surface roughness, which can be mitigated by optimizing parameters like feed rate and shielding gas.[8] Among various WAAM processes, the Gas Metal Arc Welding (GMAW)-based WAAM method is ideal and preferred for producing large metal parts[12],[13]. WAAM has become a promising technique for creating intricate metal structures on a large scale[14], [15], [16] and fabricating thin-walled parts [17]It boasts benefits including fast processing speeds, efficient use of materials, cost-effectiveness. The GMAW-based WAAM process involves generating an electric arc between the base plate and the filler wire/electrode tip, resulting in the melting and deposition of material onto the substrate [18].

1.2.1 Principles and Process Fundamentals

WAAM is classified as a Directed Energy Deposition-Arc (DED-Arc) method where an electric arc serves as the heat source to melt metal wire, which is then deposited layer by layer to build three-dimensional structures[19] The process typically employs standard welding equipment, including a power source, wire feeder, and either a robotic arm or CNC-controlled system for positioning1. The three primary variants of WAAM are Gas Metal Arc Welding (GMAW), Gas Tungsten Arc Welding (GTAW), and Plasma Arc Welding (PAW), each offering distinct advantages for specific applications.[5]

The fundamental principle involves feeding wire into an electric arc, which melts the material and deposits it onto a substrate or previously deposited layer3. The controlled movement of the deposition head, combined with layer-by-layer build strategies, enables the creation of complex geometries that would be challenging or inefficient to produce using conventional manufacturing methods.[19]

1.2.2 Process Parameters and Optimization

The quality and properties of WAAM-produced components depend critically on various process parameters, including arc current, voltage, wire feed rate, travel speed, shielding gas composition, and interpass temperature[20]. These parameters directly influence heat input, cooling rates, and consequently, the microstructure and mechanical properties of the deposited material4.

For instance, increasing energy density generally leads to deeper penetration and larger melt pools but may also result in excessive heat input causing distortion or

unfavorable microstructural changes. The travel speed significantly affects deposition rate, layer height, and cooling rate, with slower speeds typically resulting in wider beads with greater penetration.[19]

1.2.3 Advantages and Limitations

WAAM offers several significant advantages over conventional manufacturing methods and other additive manufacturing technologies. It provides exceptionally high deposition rates (3-8 kg/h) compared to powder-based methods, enabling the economical production of large components[5]. The process achieves a near-net shape with minimal material waste.

Additionally, WAAM utilizes standard welding wire, which is widely available, relatively inexpensive, and offered in numerous alloy composition[3], [5]. The equipment costs are substantially lower than those of powder-based additive manufacturing systems, making the technology more accessible for small and medium-sized enterprises.

However, WAAM also faces several challenges. The thermal history during the process leads to microstructural heterogeneity, with distinct zones having different grain structures and properties[21]. A significant limitation is the formation of large columnar grains in the as-deposited material, which can create anisotropic mechanical properties and potentially reduce performance[21]. The process also typically results in poorer surface finish and lower dimensional accuracy compared to powder-based methods, often necessitating post-processing operations[5]

1.3 NiTi and NiTiCux Alloy System

NiTi-based shape memory alloys, commonly known as Nitinol, represent the most commercially successful and widely investigated class of shape memory materials. The addition of copper to create NiTiCux systems has emerged as a promising approach to enhance specific properties and expand the application range of these alloys1213.

1.3.1 Composition and Structure

NiTi alloys typically consist of near-equiatomic compositions of nickel and titanium, with the precise Ni:Ti ratio significantly influencing transformation temperatures and mechanical properties.[5], [22] The crystal structure transforms between a high-temperature austenite phase (B2 cubic structure) and a low-temperature martensite phase (B19' monoclinic structure)[5], [22] This structural change enables the characteristic shape memory and superelastic behaviors12.

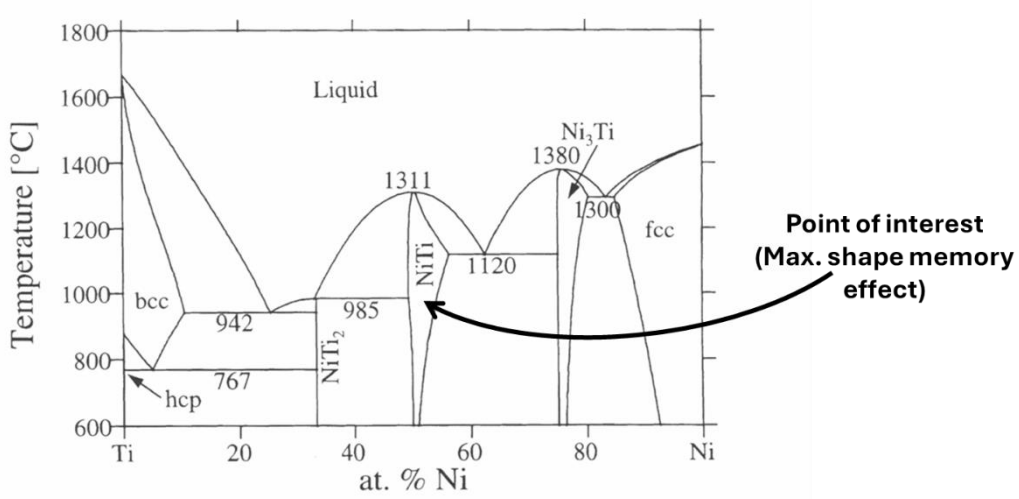

Fig. 1.7 Binary phase diagram of Ti–Ni alloy [23]

Figure 6 shows the binary phase diagram of NiTi which depicts the region for shape memory effect and states the different temperatures to perform heat treatment for playing with the composition of Ni and Ti. The NiTiCux system involves the partial substitution of nickel with copper, generally maintaining the Ti content at around 50 atomic percent[24]. The Cu substitution can range from 5 to 15 atomic percent, with different compositions yielding varying transformation characteristics[24]. In NiTiCux systems, an intermediate R-phase may appear during transformation, and at higher Cu concentrations, the martensite structure changes from B19' (monoclinic) to B19 (orthorhombic)[25].

1.4 Motivation for the Study

The development of shape memory alloys structures with controlled transformation temperature, particularly NiTi and $NiTiCu_x$ systems, represents a critical frontier in materials science and engineering. Several compelling factors drive the

exploration of Wire Arc Additive Manufacturing for these unique functional materials.

1.4.1 Limitations of Conventional Manufacturing Methods

Conventional manufacturing of NiTi and NiTiCux alloys presents significant challenges due to their high reactivity, extreme sensitivity to compositional variations, and poor machinability23. Traditional methods typically limit the production to simple forms such as wires, sheets, or tubes, constraining the potential applications of these versatile materials[25].

The processing of complex NiTi components often requires multiple steps including melting, thermomechanical processing, and extensive machining, leading to material waste, increased production costs, and compromised properties1223. Moreover, conventional techniques struggle to produce components with varying composition or properties in different regions, limiting functional design possibilities[26].

These limitations have spurred interest in alternative manufacturing approaches that can overcome these constraints while preserving or enhancing the unique properties of NiTi-based alloys.

1.4.2 Advantages of WAAM for NiTi Alloys

WAAM offers several distinctive advantages for processing NiTi and NiTiCux alloys. The process enables direct fabrication of near-net-shape components with complex geometries, reducing material waste and eliminating many of the machining operations that prove challenging with NiTi alloys[27][5]

The wire feedstock used in WAAM is more readily available and significantly less expensive than the specialized powders required for other additive manufacturing methods such as Selective Laser Melting (SLM)[27]. Additionally, wire-based processes generally achieve higher deposition rates and better material efficiency compared to powder-based techniques[27].

WAAM also offers potential advantages in terms of composition control and functional grading. By manipulating process parameters or alternating wire compositions during deposition, it becomes possible to create components with

tailored properties in specific regions[5][27]. This capability is particularly valuable for NiTi alloys, where slight compositional variations can significantly alter transformation temperatures and mechanical behavior[27].

1.4.3 Current Research Gaps

Despite the promising potential of WAAM for NiTi-based alloys, this specific application remains largely unexplored25. While other additive manufacturing methods such as SLM have been investigated for NiTi alloys[5], [22], the implementation of WAAM for these materials presents unique challenges and opportunities that warrant dedicated study25.

The additive manufacturing of NiTi SMAs is inherently complex due to the strict composition control needed for desirable phase transformation characteristics[22][5]. The thermal cycles during WAAM processing may significantly impact the microstructure, transformation behavior, and functional properties of NiTi alloys, necessitating systematic investigation of process-structure-property relationships[27].

Moreover, the addition of copper to create NiTiCux systems introduces additional complexity that has not been thoroughly examined in the context of WAAM processing[27]. Understanding how the WAAM process affects the unique properties of these alloys represents a significant knowledge gap in the field.

1.5 Objective and Scope of Study

This research aims to systematically investigate the application of Wire Arc Additive Manufacturing (WAAM) for producing NiTi and NiTiCux shape memory alloys with controlled transformation temperature, microstructure and functional properties. The study seeks to establish fundamental process-structure-property relationships and develop optimized processing strategies for these advanced functional materials.

1.5.1 Research Focus Areas

The investigation will focus on several key aspects of WAAM processing for NiTi-based alloys:

1. Process parameter optimization for achieving precise composition control and minimizing oxidation during WAAM of NiTi and NiTiCux alloys.
2. Characterization of microstructural development, including grain morphology, phase distribution, and precipitation behavior in as deposited and heat-treated conditions.
3. Evaluation of functional properties, specifically transformation temperatures, shape memory effect as functions of processing parameters and thermal history.
4. Assessment of mechanical properties, including tensile behavior, hardness.
5. Development of post-processing strategies to enhance functional properties and microstructural homogeneity of WAAM-produced NiTi and NiTiCux components.

1.6 Research Objectives

1. To study WAAM and optimize the deposition parameters using DOE and ANOVA principles.
2. To optimize the deposition of NiTi through WAAM for thin and uniform sections.
3. To analyze the effect of annealing on the microstructure, transformation temperature and hardness of the deposition.
4. To incorporate the twin-wire feed system on the in-house developed WAAM setup.
5. To select the parameter for deposition based on the transformation temperature.
6. To design and manufacture a fixture for training the clamps.
7. To deposit NiTi wall at the optimized parameters.
8. To perform heat treatment and subsequent mechanical testing on the cut thin sheet.
9. To cut the sample in thin sheets and train the sample for 90-degree actuation.
10. To study effect of Cu on the transformation temperature.

1.7 Outline of the Thesis

This thesis is organized into five chapters that systematically address the research objectives outlined above:

Chapter 1: Introduction

The introduction provides context for the research, introducing shape memory alloys, Wire Arc Additive Manufacturing, and the NiTi and NiTiCux alloy systems. It establishes motivation for the study, outlines research objectives, and presents the thesis structure.

Chapter 2: Literature Review

This chapter offers a comprehensive review of existing knowledge on shape memory alloys, their properties and applications, WAAM technology and its applications to various alloy systems, and current state of manufacturing methods for NiTi-based alloys, effect of Cu addition. The review identifies research gaps and establishes the foundation for the present work.

Chapter 3: Materials and Experimental Methods

Chapter 3 details the experimental approach, including material selection, WAAM system setup, processing parameter selection, and characterization techniques. It describes methods for microstructural analysis, mechanical testing, and functional property evaluation specific to shape memory alloys.

Chapter 4: Result and Discussion

This chapter presents the systematic investigation of WAAM process parameters and their effects on deposit quality, composition control, and microstructural development. It establishes optimal parameter windows for consistent, high-quality deposition of NiTi and NiTiCux alloys. It evaluates the shape memory effect, mechanical properties of WAAM-produced NiTi alloys in various conditions. It establishes process-structure-property relationships and identifies strategies for property optimization.

Chapter 5: Conclusions and Future Work

The final chapter summarizes the key findings of the research, discusses their implications for practical applications, identifies limitations of the current study,

and recommends directions for future research in the field of WAAM processing of shape memory alloys.

Conclusion

This thesis framework establishes a comprehensive approach to investigating the Wire Arc Additive Manufacturing of NiTi and $NiTiCu_x$ shape memory alloys. By systematically exploring process parameters, microstructural development, and resulting properties, this research aims to unlock the potential of WAAM technology for producing complex shape memory alloy components with controlled functional characteristics. The findings will contribute to the fundamental understanding of process-structure-property relationships in additively manufactured shape memory alloys and pave the way for novel engineering applications leveraging these unique materials.

Chapter 2

Literature Review

2.1 Additive Manufacturing of Shape Memory Alloys

Additive manufacturing (AM) is revolutionizing the fabrication of metallic components, including shape memory alloys (SMAs), offering significant potential to compete with or complement traditional manufacturing processes while enabling production of complex functional components[28]. Among various AM techniques developed for SMAs, wire-based methods have gained prominence due to their advantages over powder-based approaches, particularly in addressing chemical composition instability, material availability, feedstock costs, and part size limitations[29].

Wire Arc Additive Manufacturing (WAAM) has emerged as a promising technique for fabricating NiTi-based SMAs due to its cost-effectiveness, scalability, and ability to produce large components. Research published in 2022 investigated the microstructures and mechanical properties of NiTi SMAs fabricated by WAAM, demonstrating successful production of functional components with shape memory properties[30]. The study revealed that as-deposited WAAM-built NiTi exhibits superelastic behavior, except in the lower deposition zone, and both as-deposited and heat-treated samples demonstrate complete shape recovery at initial strains of 4-5%[31].

2.2 Process Parameters and Their Effects

The multi-layer deposition mechanism in ultra-high-frequency pulsed WAAM of NiTi shape memory alloys significantly influences the microstructure and functional properties of fabricated components[32]. Process parameters play a crucial role in determining deposition quality and properties. Recent research (2025) investigated the impact of processing parameters on NiTi components produced by wire laser-directed energy deposition (WL-DED), establishing optimal parameter ranges to achieve high-quality prints with minimal defects[29].

The microstructure of WAAM-fabricated NiTi typically consists of columnar millimetre-range grains growing parallel to the build direction[33]. This distinctive

microstructural characteristic significantly affects functional properties, particularly the shape memory effect and superelasticity. The layer-by-layer deposition creates complex thermal histories that further influence microstructural development and transformation behavior[27].

The core of Nitinol's functionality lies in its martensitic transformation, characterized by four critical temperatures: martensite start (Ms), martensite finish (Mf), austenite start (As), and austenite finish (Af). These temperatures define the operational window for SME and superelasticity. As illustrated in Figure 2.1a and 2.1b, even slight deviations in Ni content can dramatically shift transformation temperatures, underscoring the necessity for precise compositional control during manufacturing.

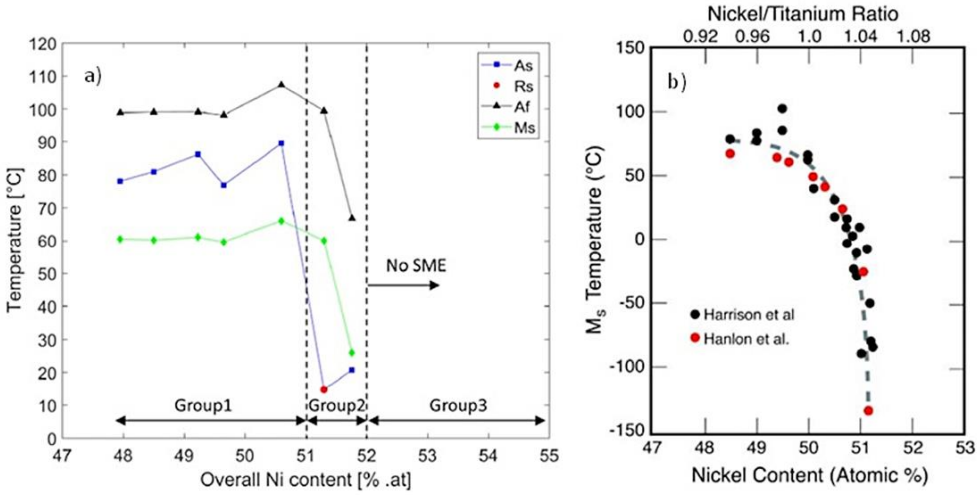

Fig. 2.1 The dependence of the TT on the Nickel content – (a), the dependence of the MS temperature on the Nickel content–(b)

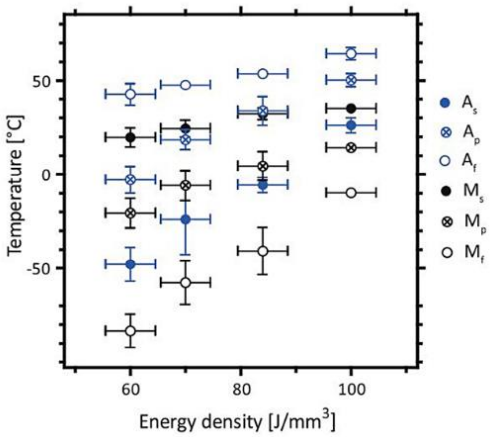

Fig. 2.2 The dependences of the temperature ranges of martensitic transformations on the energy density.

Fig 2.2 depicts the change in transformation temperature change as the energy densities change. It could be seen that as the energy densities increase the transformation temperatures also increases. So, to get higher transformation temperatures, we need to work on higher energy densities.

2.3 Post-Processing Treatments

Post-processing heat treatments are often necessary to optimize the functional properties of additively manufactured SMAs. Guimarães R et al demonstrated that solution treatment reduces chemical inhomogeneity and thermal stresses originating during deposition and cooling of NiTi components[33]. Furthermore, aging treatments at specific temperatures (350°C and 450°C) for different durations **modify superelastic behavior through precipitation of Ni4Ti3 particles[33].**

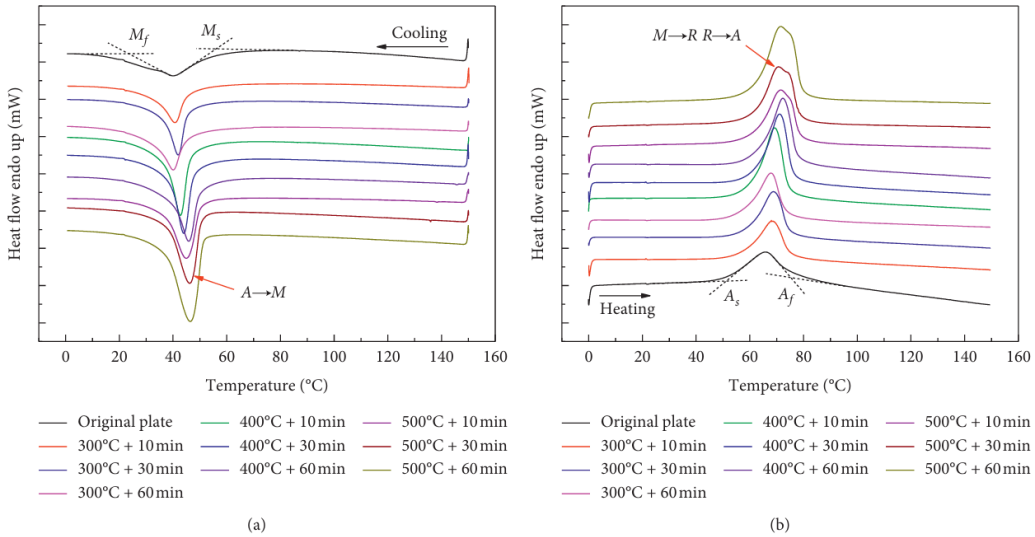

Fig. 2.3 DSC curves of the samples after thermomechanical treatment(a)Cooling (b)Heating[34]

Figure 2.3 presents typical DSC curves of samples aged at different temperatures and durations. After ageing, the phase transformation peaks became distinct and sharp. During cooling, the martensitic transformation temperatures—Ms and Mf were identified, while heating revealed the austenitic transformation temperatures—As and Af. The thermal hysteresis (As–Ms) indicates the difference between forward and reverse transformations. Samples aged at 300°C and 400°C exhibited single-stage transformations (A→M during cooling and M→A during heating). At 500°C, the R-phase appeared, with separate peaks for M→A and R→A

transformations becoming more noticeable. In Ni-rich NiTi alloys, the R-phase is typically observed during ageing at elevated temperatures.

2.4 Copper Addition to NiTi Alloys

The addition of copper to NiTi alloys (forming $NiTiCu_x$) has been explored to alter transformation behavior and mechanical properties. Research on high-Cu content NiTiCu shape memory alloys has investigated how heat treatment affects microstructural and thermal properties14. Additional studies examined transformation temperature and corrosion behavior of NiTiCu alloys, providing insights into the influence of copper addition on functional properties[35].

Copper inclusion in NiTi narrows the thermal hysteresis between transformation temperatures and improves thermal stability during cycling[35]. These characteristics make NiTiCux alloys particularly attractive for applications requiring precise temperature control and reliable cyclic performance.

2.4.1 Effects of Copper Addition

The incorporation of copper into NiTi produces several beneficial modifications to the alloy's behavior. Most notably, Cu substitution significantly reduces the transformation hysteresis, making the alloy more responsive to temperature changes and improving actuation efficiency. The transformation temperatures become less sensitive to compositional variations, allowing for more precise control and consistency in manufacturing[24].

Copper addition also reduces the matrix yield strength, which minimizes the buildup of plastic strain during cycling and improves functional fatigue resistance. NiTiCu alloys demonstrate superior thermomechanical stability during cycling compared to binary NiTi, making them particularly valuable for applications requiring repeated actuation[24].

The stress hysteresis in NiTiCux systems is narrower than in binary NiTi, resulting in reduced energy dissipation but improved reversibility. Additionally, the transformation temperature range is typically narrower, enabling more precise actuation control in temperature-sensitive applications. [24]

2.4.2 Phase Transformations and Thermal Behavior

The phase transformation sequence in NiTi and NiTiCux alloys can be complex, depending on composition, thermal history, and mechanical treatment[24]. In binary NiTi, the transformation typically proceeds directly between austenite (B2) and martensite (B19'), though an intermediate R-phase may appear under certain conditions [5], [22].

In NiTiCux systems, the transformation sequence can vary with Cu content. At lower Cu concentrations (≤10 at%), the transformation may follow B2→R→B19' on cooling, while at higher Cu contents, it tends toward B2→B19 (orthorhombic martensite) [24]. Differential Scanning Calorimetry (DSC) analysis reveals that the addition of copper generally narrows the transformation temperature range and reduces hysteresis[24]

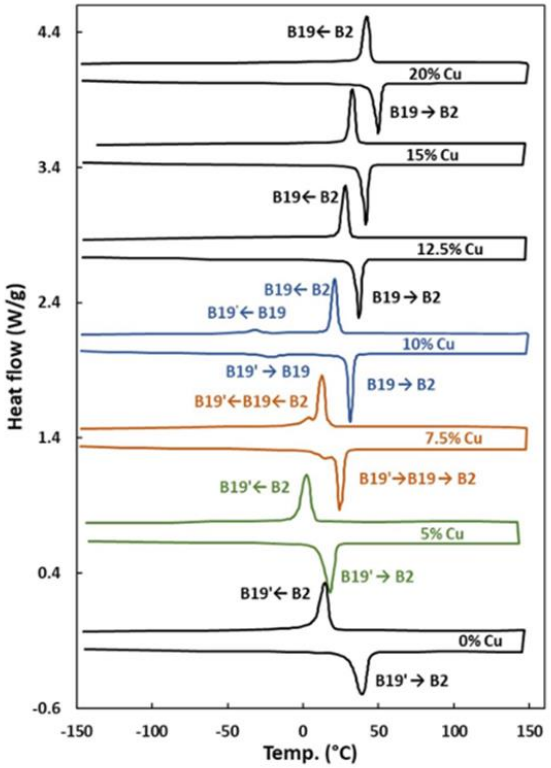

Fig. 2.4 Effect of Cu addition on transformation temperatures.[36]

Figure 2.4 displays the DSC curves of the alloys following heat treatment at 1000 °C, showing distinct thermal behaviors based on Cu content. Like binary NiTi, the 5Cu alloy exhibited a single-stage B2 ↔ B19’ transformation. Alloys with 7.5 and 10Cu showed a two-stage transformation: B2 ↔ B19 followed by B19

↔ B19'. As Cu content increased further, the second transformation was suppressed, and only the B2 ↔ B19 transition was observed in the alloys with higher Cu levels[36]. The transformation temperatures in NiTiCux alloys are influenced not only by composition but also by thermomechanical processing history[35]. Heat treatments can induce precipitation of Ni_4Ti_3 or $(Ni,Cu)_4Ti_3$ phases, which alter the matrix composition and consequently affect transformation characteristics [7]. The size, distribution, and coherency of these precipitates play crucial roles in determining the alloy's final properties[24]

2.5 Recent Advancements and Challenges

Recent advances in AM of SMAs have explored alternative techniques such as sinter-based methods. A study published in 2024 presented NiTi SMA production via Lithography-based Metal Manufacturing and Moldjet techniques, offering potential advantages in controlling microstructure and properties[37].

Despite significant progress, numerous challenges persist in AM of SMAs, including controlling chemical composition, managing microstructural heterogeneity, preventing formation of undesired secondary phases, and avoiding cracking during processing. The quest to create integral additively manufactured structures with reliable shape memory properties remains a recent and fast-emerging research frontier[38].

2.6 Training and Actuation Behavior of SMAs

Shape Memory Alloys exhibit unique properties, including the shape memory effect (SME) and superelasticity (SE), resulting from thermoelastic martensitic transformation between austenite and martensite phases. These remarkable properties make SMAs attractive for applications in aerospace, medical, automotive, and robotics industries.

Fundamental Transformation Mechanisms

The thermoelastic martensitic transformation is a diffusionless, solid-state phase transformation occurring in SMAs upon changes in temperature or applied stress. This transformation involves reversible atomic movements over distances smaller than interatomic spacing, resulting in crystal structure changes without altering

chemical composition. Research employing lattice Monte-Carlo simulations has investigated the combined influence of external stress, temperature, and interface energy between austenitic and martensitic phases on transformation kinetics and material compliance[39].

SMAs possess several desirable properties, including high actuation power, large recovery strain, pseudoelasticity, good chemical resistance, and biocompatibility. The one-way shape memory effect allows SMAs to recover their original shape upon heating after deformation in the martensitic state, while superelasticity enables large reversible strains through stress-induced martensitic transformation at temperatures above the austenite finish temperature[40].

Training Methods for Shape Memory Effect

Training of SMAs is essential for achieving controlled actuation behavior, particularly for developing the two-way shape memory effect (TWSME). Unlike the one-way effect, TWSME enables SMAs to remember two distinct shapes: one at high temperatures (austenite phase) and another at low temperatures (martensite phase)[41]. This capability is particularly valuable for applications requiring reversible actuation without external forces.

Research has investigated various thermomechanical training procedures for inducing TWSME in NiTi alloys. A study published in 2023 applied predefined thermomechanical procedures to study the effect of different applied load conditions on the induced martensitic state. Results revealed that inducing internal stresses along specified directions during training cycles results in formation of oriented martensitic variants rather than twinned martensitic variants upon cooling[41].

The training process introduces permanent microstructural changes that create internal stresses, guiding formation of specific martensitic variants during cooling. These internal stresses serve as memory elements, enabling the material to remember both high-temperature and low-temperature shapes. A study on SMA-based actuators with TWSME proposed a training method that enables them to shorten and extend through heating and cooling cycles[42].

Effect of Heat Treatment on Actuation Properties

Heat treatment significantly influences the actuation behavior of SMAs by altering transformation temperatures, microstructure, and mechanical properties. Research on NiTi wires has investigated the effect of heat treatment parameters on actuation performance. A study published in 2023 examined the effect of heat treatment time and temperature (400-500°C for 30-120 min) on the microstructure and shape memory properties of Nitinol wires[43].

This research revealed that DSC analysis showed a decrease in austenite transformation temperature from 42.8°C to 24.39°C with increasing heat treatment temperature from 400°C to 500°C, attributed to the formation of Ni4Ti3 precipitates16. Conversely, increasing heat treatment time led to an increase in austenite transformation temperature. The relationship between hardness and heat treatment temperature was found to be negative, attributed to the formation and growth of precipitates affecting matrix properties[43].

Similarly, research on NiTi orthodontic closed coil springs determined that the optimum heat treatment parameter was 500°C for 40 minutes, producing appropriate force delivery levels and relatively low plateau slopes17. The thermo-mechanical properties were significantly influenced by heat-treatment temperature rather than duration, with 500°C treatments showing superelastic tendency with lower stress hysteresis[44].

Challenges in SMA Actuation

Despite significant progress in understanding and developing SMA actuators, several challenges persist in achieving reliable and consistent actuation behaviour. These include managing functional fatigue during cyclic actuation, controlling transformation temperatures precisely, and optimizing energy efficiency of SMA actuators. For additively manufactured SMAs, these challenges are compounded by microstructural heterogeneity resulting from the layer-by-layer deposition process. Research on thermocycling influence on functional properties of WAAM-produced NiTi alloys demonstrated that variation in martensitic transformation temperatures depends on chemical composition of the layer. Transformation temperatures decreased during thermal cycling in Ti-rich NiTi layers, whereas they remained constant in Ni-rich NiTi layers[45].

Chapter 3

Materials and Methods

3.1 Material Specification

NiTi wire of diameter 1.2 mm was utilized for the study. The wire was deposited on a Ti substrate of 15 mm thickness. The composition of wire was checked using EDS and is tabulated in Table 1.Fig. 3.1 shows the microscopic image of NiTi wire utilized for deposition.

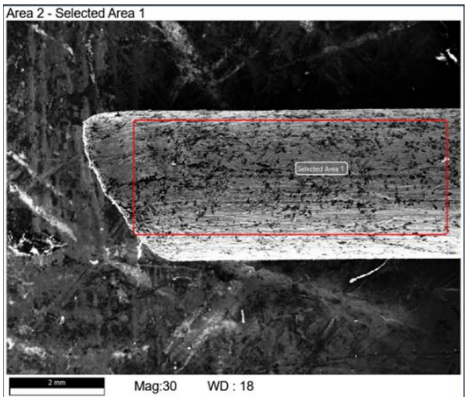

Fig 3.1 Microscopic image of NiTi wire

Table 3.1 Composition of NiTi wire

Element	Weight %	MDL	Atomic %	Error %
Ti K	44.0	1.52	49.1	4.2
Ni K	56.0	4.23	50.9	4.9

Table 3.2 Mechanical properties of deposited NiTi samples

Characteristic	Units	Value
Density	g/cm^3	5.5 * 10^-3
Modulus of elasticity (Martensite)	MPa	822
Poisson's ratio	—	0.33
Yield strength (Martensite)	MPa	200

Table 3.2 depicts the mechanical properties of the NiTi deposition which has been calculated experimentally.

3.2 WAAM Process and Parameter Study

In-house developed Wire Arc Additive Manufactured (WAAM) setup was employed in the present study for deposition, as shown in Figure 3.2, with its schematic shown in Figure 3.3. The WAAM system includes a welding torch, wire feeder, and motorized XYZ stage for deposition. The wire feeder supplies the wire to the torch, while the X-Y stage moves the torch during layer formation. The X-Y stage movement is controlled by G and M codes, with the M code being controlled by the Repitier host device.

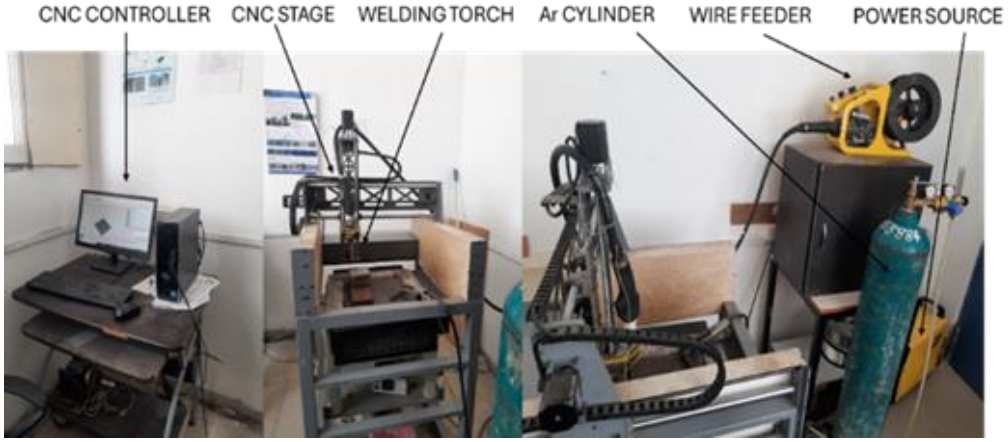

Fig. 3.2 Experimental Setup of GMAW-WAAM

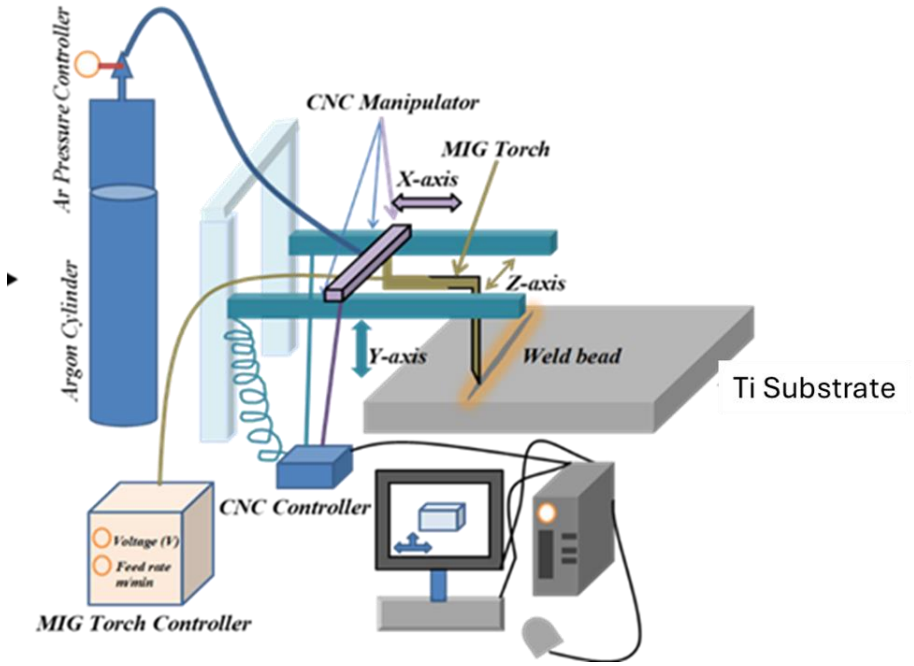

Fig. 3.3 Schematic of GMAW-WAAM

3.2.1 Screening Design and Full Factorial Design

A fractional factorial design approach was employed for preliminary tests and screening design to systematically vary the parameters and evaluate their effects. Three levels for each parameter were chosen. After screening, the remaining parameters were varied based on the full factorial design. A design matrix was generated based on these two (voltage and wire feed rate) process parameters, and these parameters (factors) varied at three levels. Additionally, ANOVA was employed to determine the significance of individual input parameters on independent output responses. The weld bead height, bead width and aspect ratio were measured as responses, and further analysis was conducted using MINITAB statistical software.

Initially, a single layer deposition was done, and after understanding the effect of parameters on the geometry of beads, a multilayer deposition (wall deposition) was done. A single layer deposition was done while varying the wire feed rate, argon flow rate and voltage. Parameters such as scan speed and stand-off distance are set at 8.57 mm/s and 15 mm, respectively. For single layer analysis, voltage, argon flow rate, and wire feed rates are varied within ranges of 13–17 V, 10-20 L/min, and 3–5 m/min, respectively. After analyzing the results, it was found that argon flow rate does not significantly affect the deposition geometry. Therefore, voltage and wire feed rate are only varied for wall deposition, using full factorial design. For wall deposition, voltage is set in the range of 13-17 V and wire feed rate at 3-5 m/min. A dwell time of 4 s between layers is used to build wall structures.

3.3 Microstructural and Compositional Analysis

Samples are prepared following standard metallographic procedures. The microstructure is examined with a scanning electron microscope (ZEISS Gemini SEM 360, Germany). The phase analysis is done through XRD (PANalytical Empyrean) followed by Xpert HighScore software.

Sections of the WAAM deposited sample were used to create the specimens for microstructure analysis, as illustrated in Figure. The specimens were polished to 2000 grit paper and then polished with 1 μm and 0.25 μm paste of diamonds. Keller's reagent was used to chemically etch the samples for 25 seconds, and an

inverted optical microscope was used to view the microstructure. Table 2.3 below displays the composition of the Keller's reagent.

Table 3.3 Keller's reagent composition

Ingredients	Distilled water	Nitric Acid (HNO_3)	Hydrochloric Acid (HCL)	Hydrofluoric Acid (HF)
Volume (ml)	190	5	3	2

The WAAM deposited sample is studied using various characterization techniques for material confirmation. The morphological characterization is performed using Field Emission Scanning Electron Microscopy (FE-SEM) and physical characterization of material is performed using Energy Dispersive Spectroscopy (EDS) and X-Ray diffraction.

3.3.1 Field Emission Scanning Electron Microscopy (FESEM):

To study morphology and its variations over the different energy variations, FE-SEM is used. It is a high-resolution technique where electron beam emitted by field emission source strikes the surface of the sample placed under it. It is then raster scanned to obtain microstructure and surface morphology at varying magnifications.

Figure 3.4 Field Emission Scanning electron microscope (FE-SEM)

The inner arrangement of setup is such that the ejected electron beam passes through an arrangement of magnetic lenses and metal apertures in a vacuum tube for focusing as a thin monochromatic beam. when incident electron beam interacts with sample, it generates output beams in the form of backscattered electrons, secondary electrons, Auger electrons and characteristic X-rays with different detectors collecting each type of electron and hence produces images of the sample specimen. the elastic interaction between sample and electron beam excelling out of source leads to back scattered electrons creations. However, there are electrons which do not interact with nucleus of the specimen are reflected back or backscattered from the sample. it is observed that backscattered electron depends on the atomic weight of element. Due to stronger deflection from bigger nucleus, the element with higher atomic mass generates higher number of backscattered electrons. It gives a better information of composition and topography of the sample.

The inelastic interaction between sample and electron beam generates secondary electrons. due to loss of inelastic interaction, the energy is less than backscattered electrons. The secondary electron detector is positioned at an angle to the axis of incident beam to improve the efficiency of detector. Secondary electrons help to study the surface morphology of sample. In this study, a Field-emission scanning electron microscope (FE-SEM, JEOL JSM-7400F) as shown in the Fig. 3.4, is employed to study the morphology of WAAM deposited sample.

3.3.2 Energy Dispersive Spectroscopy (EDS)

Energy Dispersive Spectroscopy (EDS) is an analytical technique utilized alongside scanning electron microscopy (SEM) to determine the elemental composition of materials. By bombarding a sample with a focused electron beam in the SEM, EDS detects characteristic x-rays emitted from the sample's atoms. When the high-energy electrons displace inner-shell electrons, subsequent electron transitions emit x- rays with energies specific to the elements present. These emitted x-rays are captured by an energy-dispersive detector, which records their energies. The resulting energy spectrum reflects the elemental composition of the sample. Through spectral analysis, peaks in the spectrum are correlated with known elemental standards to identify the elements within the sample. EDS is invaluable

in fields like materials science, geology, forensics, and biology, offering insights into a sample's chemical makeup, distribution, and morphology at the microscopic level. Its non-destructive nature and high sensitivity make it a versatile tool for a wide range of applications, from identifying trace elements in geological samples to characterizing the elemental composition of biological tissues. EDS facilitates detailed analysis, aiding researchers in understanding the properties and behavior of diverse materials. In this study, the compositional analysis of WAAM deposited sample and laser nitride sample was carried out using Energy Dispersive Spectroscopy (EDS) which was coupled with the FE-SEM as shown in Fig. 3.4.

3.3.3 X-Ray Diffraction

Fig. 3.5 X-ray diffractometer using Cu-Kα radiation.

X-Ray diffraction technique is a non-destructive often used to identify and analyze the crystal structure, degree of crystallinity and availability of impurity phases if any**.** It works on the principle that when a high- energy beam falls over a target material, energy absorption happens, and electrons jumps from inner to outer shell

thus in an unstable state condition. Due to natural tendency of electrons to reach back to initial stable state, the electrons come back to its original state thus releasing X-rays. The electrons moving from M shell to K shell generates Kβ x- rays and the ones moving from L shell to K shell generates Kα x-rays. The basic principle of analysis of XRD is based on Bragg's law as shown in the Fig. 3.5 which states that "When a collimated beam of x-rays strikes a crystal, the atoms act as diffraction

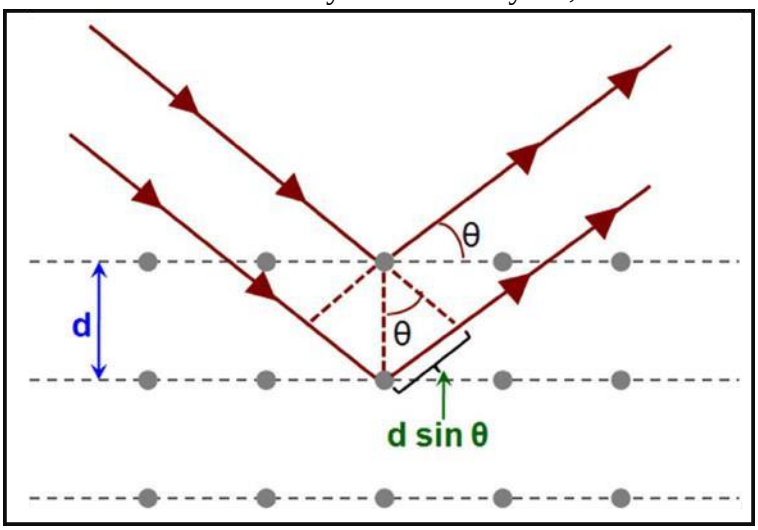

centers and the diffracted beams combine to give diffraction patterns.".

Fig 3.6 Bragg's Law in a 2-D crystal

For n^{th} order diffraction, using the X-rays of wavelength λ, the Bragg's equation is:

$$n\lambda = 2d \sin\theta \quad \text{..... (3.1)}$$

The phases were studied using Grazing Incidence X-Ray Diffraction (GI-XRD) by Cu-Kα radiation at an incident angle of 3◦.

3.5 Transformation Temperature Measurements

The transformation temperature analysis was done using a DSC setup (Netzsch STA449F3) having a range of -200 °C to º550 C, with a heating and cooling rate of 10 °C/min.

3.6 Mechanical Testing

The microhardness at 10 N load is determined using a Vickers microhardness tester (Econometer VH-1MDX) with a 10 s dwell period. The tensile testing was done using a universal tensile testing machine having a maximum load of 2kN.

3.6.1 Tensile Testing

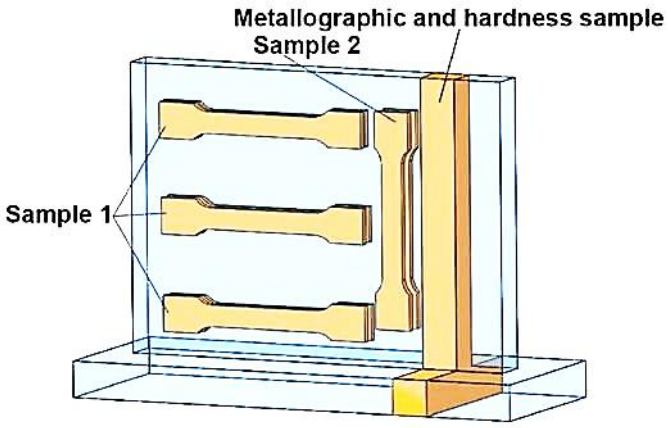

Fig. 3.7 Schematic diagram of the additively manufactured part representing the positions of the tensile, metallographic and micro-hardness test samples

The tensile test samples were made by sectioning the WAAM deposited wall by wire cut EDM as shown in Figure 3.7. As seen in Figure 3.7, the samples were made in two directions: parallel to the substrate and perpendicular to the substrate. A universal tensile tester machine was used to perform the tensile test at room temperature and 120 ºC at loading rate of 1.5 mm/min.

3.6.2 Microhardness Testing

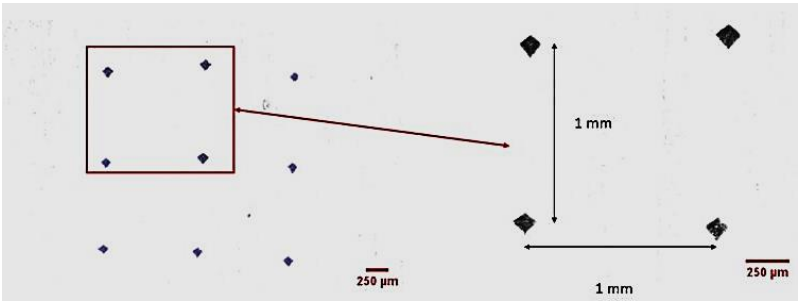

Fig. 3.8 Vickers Micro-Hardness Test Indentation Images

Micro-hardness testing was performed using Micro Vickers VH-1MDX (Economet VH-1MDX) with 200 g load and 15 s dwell time at the middle section of each sample at 5 different locations and the average of these values was reported.

Fig. 3.9 Vickers Micro-Hardness Testing setup

Apart from that the micro-indentation for micro hardness measurement of the WAAM deposited sample under optimal parametric setting, is observed along the deposition with 1 mm interval as shown in the Figure.

3.7 Heat Treatment Procedures

The heat treatment of the samples including homogenization, solutionizing and aging was done using a muffle furnace with a heating rate of 10 ºC/min and a temperature limit of 1200 °C.

3.8 Cu Addition and Its Effect

The copper addition is done through a twin wire set-up designed and developed in-house.

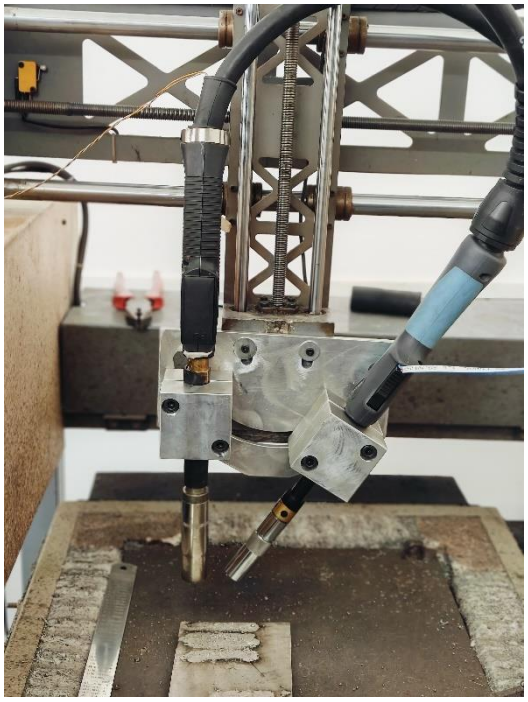

Fig. 3.10 Twin torch setup designed for Cu addition

3.9 Sheet Cutting and Training for Actuation

The wire-cut electrical discharge machine(wire-EDM) is utilized for cutting the deposition perpendicular to the laying direction. After cutting the samples, the training is done in a muffle furnace.

Different mechanical testing like Micro-Hardness test and Micro Tensile test are performed on the WAAM deposited sample and laser nitrided sample and it's effects are studied.

Chapter 4

Results and Discussion

4.1 WAAM Process Optimization

4.1.1 Single layer deposition of SS-304 on low-C steel substrate

Using the GMAW-WAAM setup, a single layer deposition was done based on fractional-factorial design of experiments for screening. The process parameters such as voltage (13, 15, 17 V), wire feed rate (3, 4, 5 m/min) and argon flow rate (10, 15, 20 L/min) were varied at three levels, and the combinations of the parameters are mentioned in Table 4.1. Figure 4.1 shows the digital image of the single layer deposition.

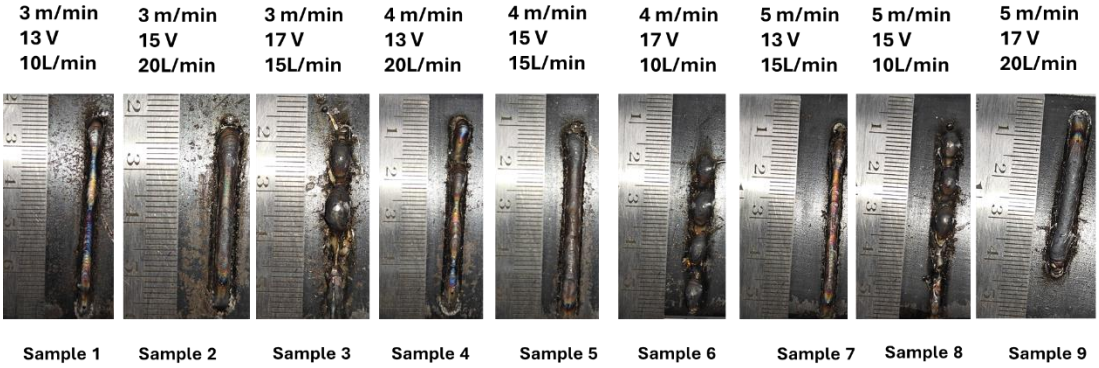

Fig.4.1 Single track deposition of SS-304 on a low C steel substrate

Table 4.1. Width of beads on different parameters designed using fractional factorial screening design

No.	Sample No.	Feed Rate (m/min)	Voltage (Volts)	Argon Flow Rate (L/min)	Response (Width) (mm)
1	1	3	13	10	3
2	7	3	15	20	2.4
3	4	3	17	15	2.9
4	8	4	13	20	4.6

5	5	4	15	15	3.1
6	2	4	17	10	3.3
7	6	5	13	15	5.4
8	3	5	15	10	4.9
9	9	5	17	20	3.6

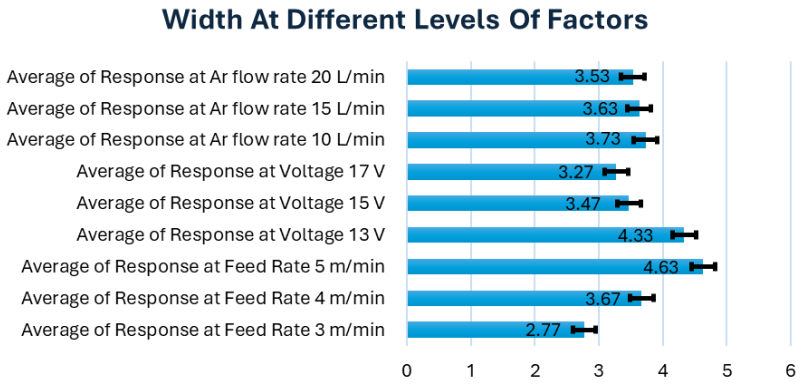

Fig. 4.2 Bead Width at different levels of parameters

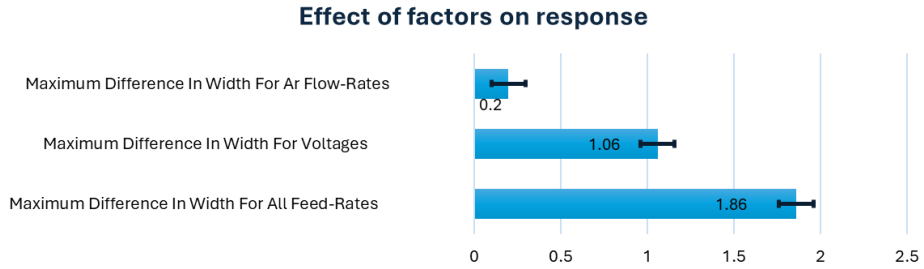

Fig. 4.3 Effect of factors on response(width)

Figure 4.2 depicts the average width at different levels of each parameter. Figure 4.3 indicates that the flow rate of argon has minimal impact on the width of the bead, while both voltage and wire feed-rate significantly influence the width of the deposition. Argon flow rate is primarily used to establish an inert atmosphere for deposition and prevent oxidation. Thus, it does not directly impact the geometry of the deposition. So, for the purpose of multibead deposition (wall deposition), only voltage and wire feed rate were varied in the study and their effect was studied.

4.1.2 Multi-layer(10 layers) deposition of SS-304 on low-C steel substrate

A ten-layer deposition was done at different values of wire feed rate and voltage to build a wall structure. The process parameters i.e voltage (13, 15, 17 V) and wire feed rate (3, 4, 5 m/min) were varied at three levels, and the combinations of the parameters are mentioned in Table 4.2. The design was done using a full-factorial design with one replication. Figure 4.4 shows the image of the multi-layer deposition of the SS-304L. It can be observed that a uniform deposition was obtained, particularly at a wire feed rate of 3 m/min with voltages of 15 V, 17 V, and 4 m/min with a voltage of 17 V. This combination of parameters defines the process window for achieving uniform deposition. It was found that the deposition was not uniform in all other cases, indicating that certain combinations of wire feed rate and voltage did not result in uniform deposition.

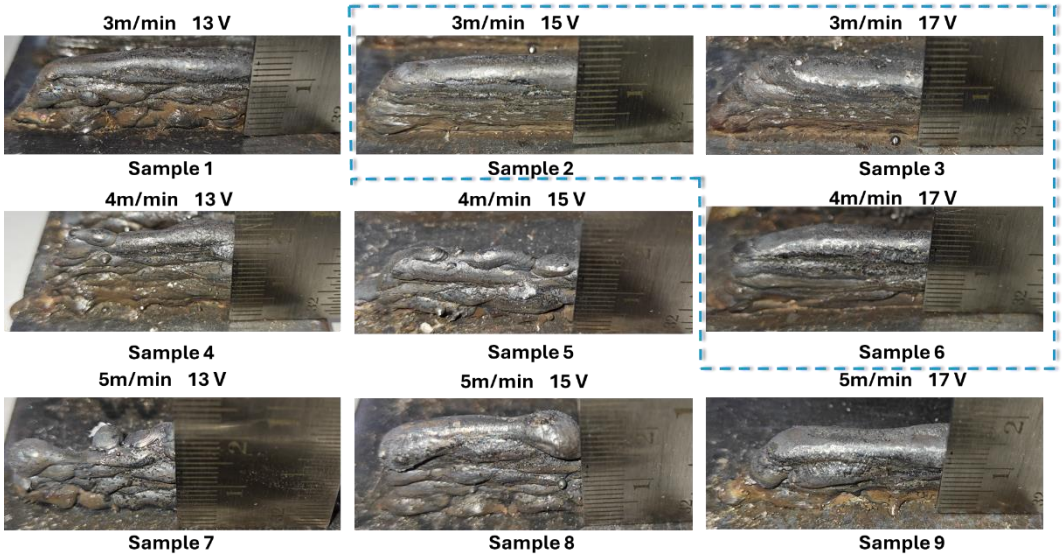

Fig.4.4 Multilayer deposition (10 layers)

Table 4.2. Geometry of deposition at different parameters designed using full factorial design.

No.	Wire Feed Rate (m/min)	Voltage (Volts)	Width (mm)	Height (mm)	Aspect Ratio
1	3	13	3.9	15	3.846

2	3	15	5.5	13	2.364
3	3	17	4.8	13	2.708
4	4	13	5	17	3.400
5	4	15	6.2	16	2.581
6	4	17	4.8	13	2.708
7	5	13	7.7	17	2.208
8	5	15	7.4	18	2.432
9	5	17	6.2	12	1.935
10	3	13	5.6	13	2.321
11	3	15	5.4	11	2.037
12	3	17	5.9	10	1.695
13	4	13	4.9	16	3.265
14	4	15	6.4	13	2.031
15	4	17	6	14	2.333
16	5	13	7.4	16	2.162
17	5	15	6.9	13	1.884
18	5	17	7.1	11	1.549

4.1.3 Effect of WAAM parameters on Aspect-Ratio of deposition

To understand the influence of each parameter independently and their combined effect on the aspect-ratio of deposition ANOVA is employed. To understand the fit of the ANOVA model, R-squared and Adjusted R-squared values were studied. R-squared (R-sq) is a measure of the proportion of variance in the dependent variable explained by the independent variables in an ANOVA model. A high R-sq value signifies a greater explanation of variability in the dependent variable. Adjusted R-squared(R sq(adj)) is commonly utilized in ANOVA models with multiple independent variables

as it provides a more accurate reflection of the model's explanatory power compared to regular R-sq.

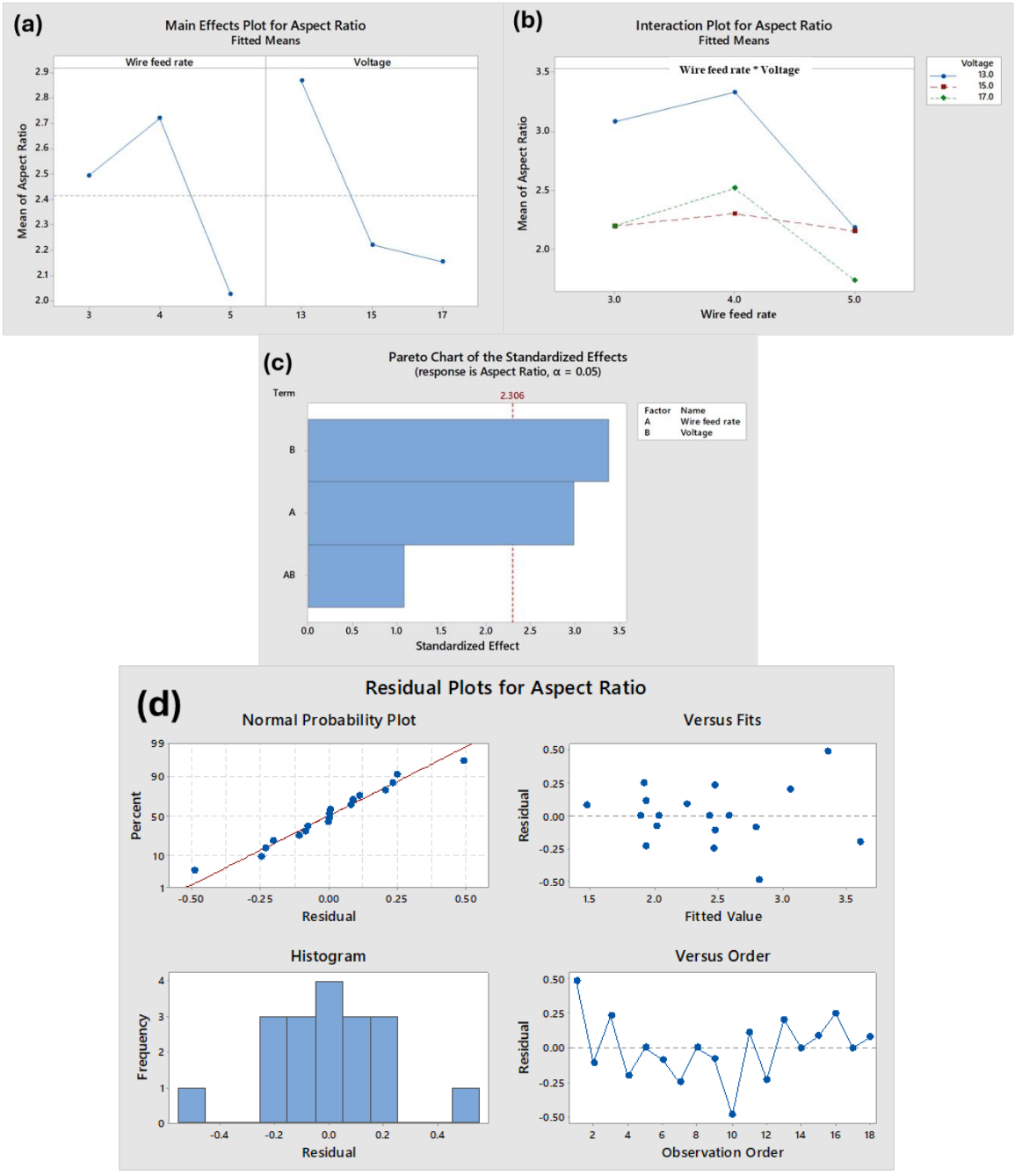

Fig 4.5. (a) Main effect plot for aspect ratio (b) Interaction plot for aspect ratio (c)Pareto chart for aspect ratio (d)Residual plots for aspect ratio

Figure 4.5(a) indicates that the aspect ratio decreases as voltage increases, possibly due to the power of deposition increasing with voltage, leading to enhanced weld pool fluidity and a decrease in aspect ratio. The wire feed rate initially increases the aspect ratio by providing more material for deposition, but then decreases due to excess material, constant travel speed, increased power, and increased gravitational effects. In Figure 4.5(b), the graph displays non-parallel lines, suggesting an interaction between wire feed rate and voltage but the interaction is not very significant, which can be seen from Pareto chart shown in Figure 4.5(c). From Table 4.3, it can be observed that the R-sq value is above 70%, thus the model demonstrates a satisfactory fit. This can also be validated from residual plots shown in Figure 4.5(d).

Table 4.3. Model Summary

S	R-sq	R-sq(adj)
0.325794	86.16%	70.59%

Aspect Ratio = 2.4144 + 0.081 Wire feed rate_3 + 0.305 Wire feed rate_4
- 0.386 Wire feed rate_5 + 0.453 Voltage_13 - 0.193 Voltage_15
- 0.260 Voltage_17 + 0.136 Wire feed rate*Voltage_3 13
- 0.102 Wire feed rate*Voltage_3 15
- 0.034 Wire feed rate*Voltage_3 17
+ 0.160 Wire feed rate*Voltage_4 13
- 0.221 Wire feed rate*Voltage_4 15
+ 0.061 Wire feed rate*Voltage_4 17
- 0.296 Wire feed rate*Voltage_5 13
+ 0.323 Wire feed rate*Voltage_5 15
- 0.027 Wire feed rate*Voltage_5 17 ---------- (4.1)

The regression equation 4.1 is used to establish relationship between the dependent variable (aspect ratio) and independent variables (voltage, wire feed rate).

4.1.4 Effect of WAAM parameters on Width of deposition

To understand the impact of each parameter independently and their combined effect on the width of deposition, ANOVA is employed. To understand the fit of the ANOVA model, R-squared and Adjusted R squared values are studied.

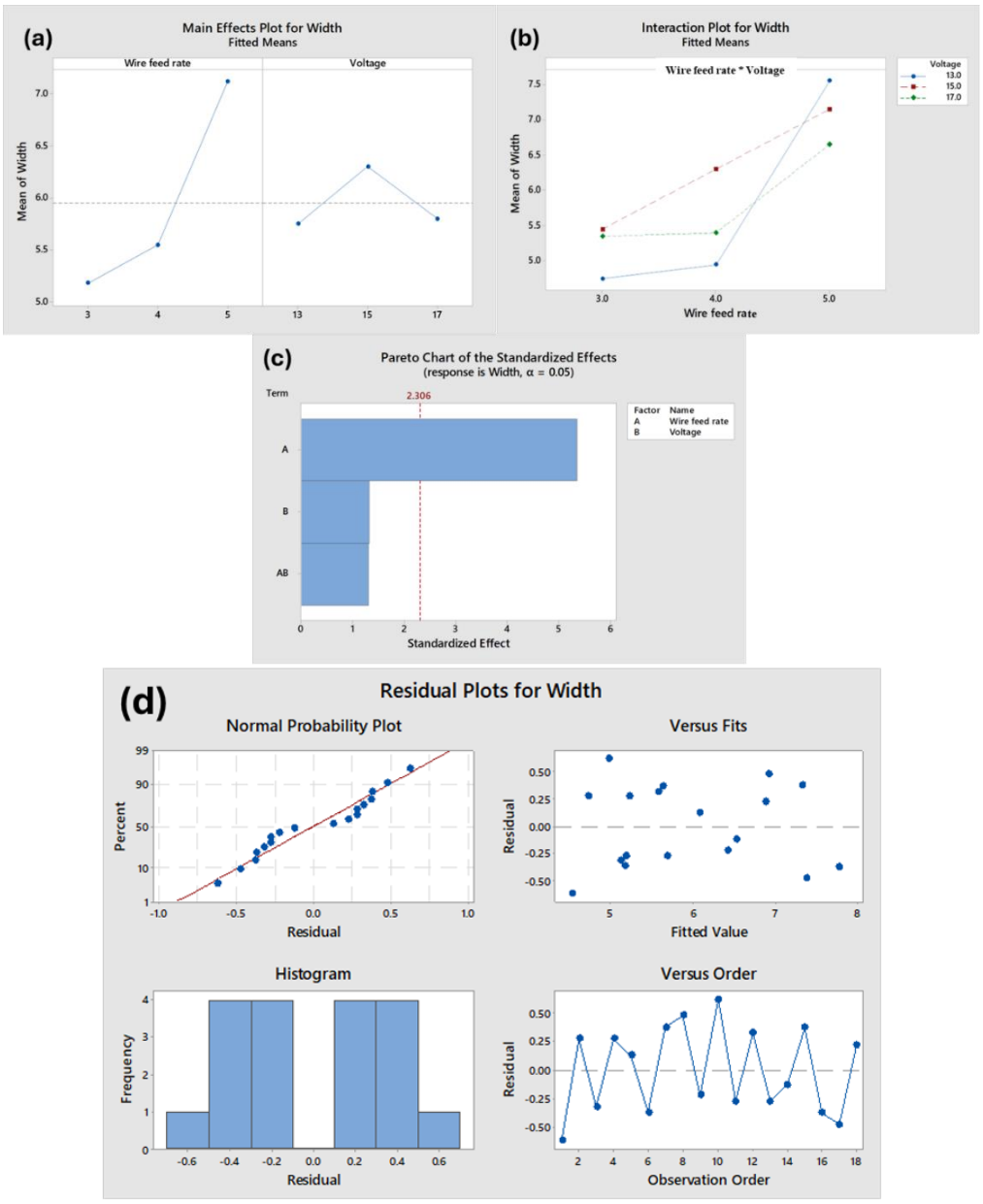

Fig 4.6 (a)Main effect plot for width (b)Interaction plot for width (c)Pareto chart for width (d)Residual plots for width

Figure 4.6(a) indicates that the width increases as the wire feed rate increases, while voltage has no impact on the width. WAAM utilizes high heat inputs, resulting in rapid cooling rates. This can constrain the lateral spread of the molten pool, thereby restricting the influence of voltage on weld width. Increasing the wire feed rate leads to a wider deposition by enhancing weld pool fluidity and gravitational effects. In Figure 4.6(b), the graph displays non-parallel lines, suggesting an interaction between wire feed rate and voltage but the interaction is not very significant, which can be seen from the Pareto chart in Figure 4.6(c). From Table 4.4, it can be observed that the R-sq value is above 70%, thus the model demonstrates a satisfactory fit. This can also be validated from residual plots shown in figure 4.6(d).

Table 4.4 Model Summary

S	R-sq	R-sq(adj)
0.552394	87.36%	73.13%

Wid = 5.950 - 0.767 Wire feed rate_3 - 0.400 Wire feed rate_4
th + 1.167 Wire feed rate_5
- 0.200 Voltage_13 + 0.350 Voltage_15 - 0.150 Voltage_17
- 0.233 Wire feed rate*Voltage_3 13 - 0.083 Wire feed rate*Voltage_3 15
+ 0.317 Wire feed rate*Voltage_3 17 - 0.400 Wire feed rate*Voltage_4 13
+ 0.400 Wire feed rate*Voltage_4 15 - 0.000 Wire feed rate*Voltage_4 17
+ 0.633 Wire feed rate*Voltage_5 13 - 0.317 Wire feed rate*Voltage_5 15
- 0.317 Wire feed rate*Voltage_5 17
---------- (4.2)

The regression equation 4.2 is used to establish relationship between the dependent variable (width) and independent variables (voltage, wire feed rate).

4.1.5 Effect of WAAM parameters on Height of deposition

To understand the impact of each parameter independently and their combined effect on the height of deposition, ANOVA is employed. To understand the fit of the ANOVA model, R-squared and Adjusted R squared values are studied.

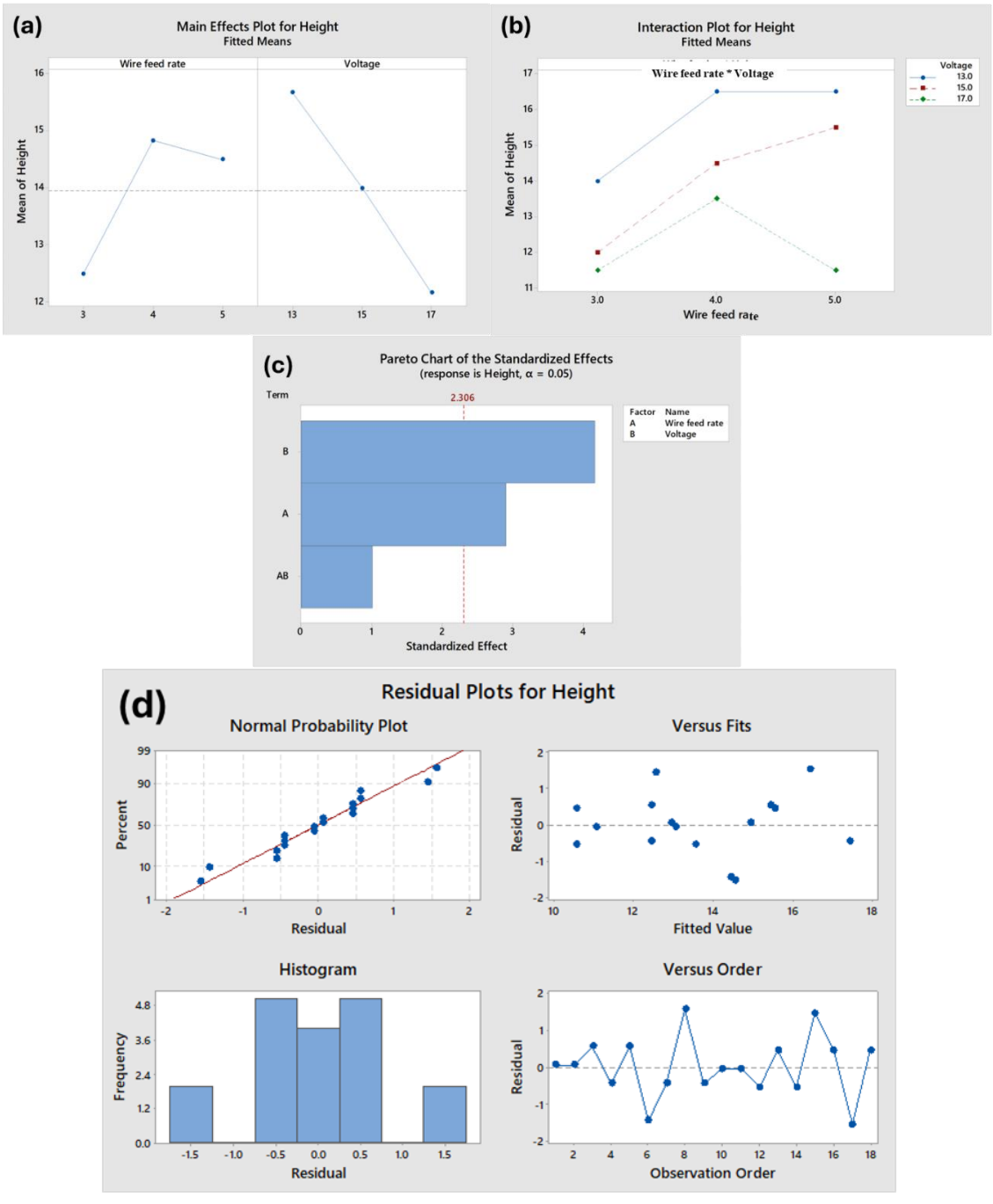

Fig 4.7 (a)Main effect plot for height (b)Interaction plot for height (c)Pareto chart for height (d)Residual plot for height

From Figure 4.7(a), the relationship between height and voltage shows a decreasing trend, while the relationship between height and wire feed rate initially increases and then slightly decreases. The decrease in height with increasing voltage can be attributed to the enhanced fluidity of the weld pool. On the other hand, the initial increase in height with increasing wire feed rate is due to the availability of more material, followed by a decrease caused by an excess of material and melt pool fluidity.

Table 4.5. Model Summary

S	R-sq	R-sq(adj)
1.19606	87.42%	73.26%

From Table 4.5, it can be observed that the R-sq value is above 70%, thus the model demonstrates a satisfactory fit. In Figure 4.5(b), the graph displays non-parallel lines, suggesting an interaction between wire feed rate and voltage but the interaction is not very significant, which can be seen from the Pareto chart in Figure 4.5(c).

Height = 13.944 - 1.444 Wire feed rate_3 + 0.889 Wire feed rate_4
+ 0.556 Wire feed rate_5
+ 1.722 Voltage_13 + 0.056 Voltage_15 - 1.778 Voltage_17
- 0.222 Wire feed rate*Voltage_3 13 - 0.556 Wire feed rate*Voltage_3 15
+ 0.778 Wire feed rate*Voltage_3 17 - 0.056 Wire feed rate*Voltage_4 13
- 0.389 Wire feed rate*Voltage_4 15 + 0.444 Wire feed rate*Voltage_4 17
+ 0.278 Wire feed rate*Voltage_5 13 + 0.944 Wire feed rate*Voltage_5 15
- 1.222 Wire feed rate*Voltage_5 17
---------- (4.3)

The regression equation 4.3 is used to establish relationship between the dependent variable (height) and independent variables (voltage, wire feed rate).

4.1.6 Response Optimization: Height, Width, and Aspect Ratio Parameters

Response optimization i.e maximizing the aspect ratio, minimising the width and maximizing the height was done based on the ANOVA model using MINITAB software. For optimization, the process window shown in Figure 4.4 was taken. Table 4.6 shows the values of parameters for optimization.

Table 4.6 Parameters for optimization

Response	Goal	Lower	Target	Upper	Weight	Importance
Height	Maximum	10.000	18.0		1	1
Width	Minimum		3.9	7.7	1	1
Aspect Ratio	Maximum	1.549	2.8		1	1

Table 4.7 Solution of optimization

Solution	Wire feed rate	Voltage	Height Fit	Width Fit		Aspect Ratio Fit	Composite Desirability
1	4	17	13.5	5.4		2.5205	0.590250

It can be seen from Table 4.7, that a voltage of 4V and a wire feed rate of 17V are the optimized result as per our ANOVA model and these parameters will be used for further deposition and its analysis.

4.2 Laser-hybrid WAAM

After optimizing the deposition by GMAW-WAAM, we want to further increase the aspect-ratio and decrease the width of deposition. Laser-hybrid WAAM can lead to our desired results as it will confine the melt pool in a specific region and thus help in reducing the width of the deposition to produce thin sections.

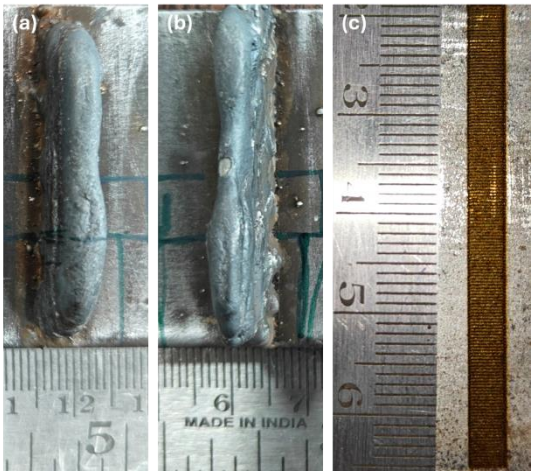

Fig.4.8 (a)GMAW-WAAM Deposition (b) Laser-hybrid WAAM Deposition (c) Laser marked substrate

Figure 4.8(a) shows the top view of a ten-layer wall deposition by GMAW-WAAM whereas Figure 4.8(b) shows the top view of a ten-layer wall deposition by Laser-hybrid deposition. Figure 10(c) shows the laser marked surface created by a 50W, 1064 nm wavelength, fiber laser for laser-hybrid deposition.

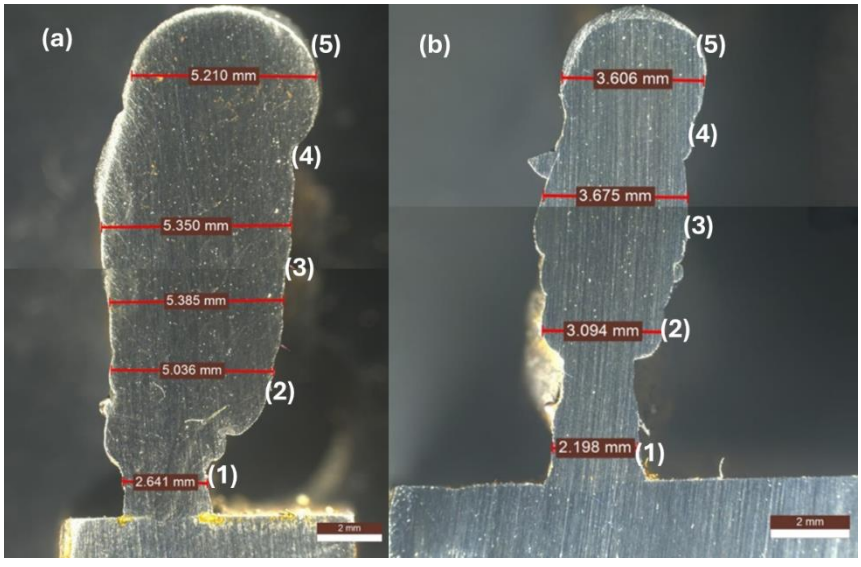

Fig 4.9(a) Profile of GMAW-WAAM deposition (b)Profile of Laser-hybrid deposition

Figure 4.9(a) shows the cross section of ten-layer wall deposition by GMAW-WAAM and Figure 4.9(b) shows the cross section of ten-layer wall deposition by Laser-hybrid WAAM. The deposition from laser-hybrid WAAM seems more uniform.

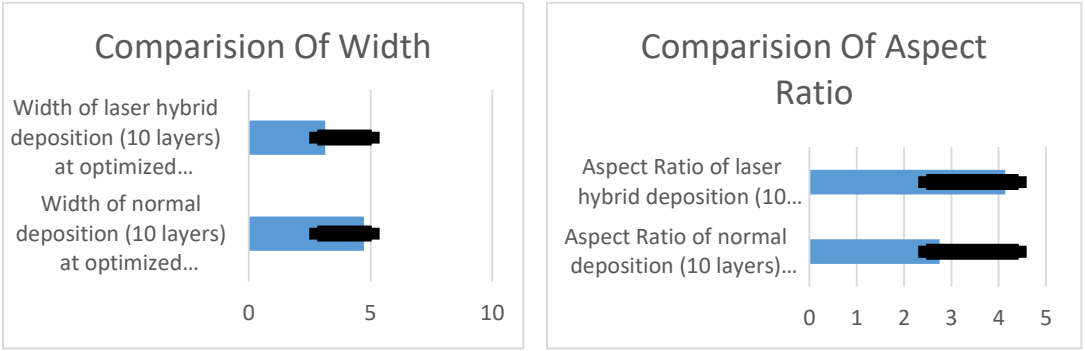

Fig.4.10 (a)Comparison of width of GMAW-WAAM and Laser-hybrid WAAM (b) Comparison of Aspect-ratio of GMAW-WAAM and Laser-hybrid WAAM

Figure 4.10(a) shows that the width of deposition by GMAW-WAAM is more than the Laser-hybrid WAAM deposited sample and Figure 4.10 (b) shows that the aspect-ratio of GMAW-WAAM deposition is less than the Laser-hybrid WAAM deposition. The possible reason to this could be the melt pool confinement due to the laser marked surface and efficient heat transfer due to increase in surface area. Table 4.8 shows the numerical values of the width and aspect-ratio.

Table 4.8 Geometry of deposition of wall by GMAW-WAAM and Laser-hybrid WAAM

Width of normal deposition (10 layers) at optimized parameters	4.7244 mm
Width of laser hybrid deposition (10 layers) at optimized parameters	3.1432 mm
Aspect Ratio of normal deposition (10 layers) at optimized parameters	2.7517 mm

Aspect Ratio of laser hybrid deposition (10 layers) at optimized parameters	4.1359 mm

Laser-hybrid WAAM shows a promising result, decreasing width of the deposition by 33.5% and increasing aspect ratio of deposition by 50.3%, hence laser hybrid WAAM can be used to produce components with thin sections.

4.2.1 Effect of substrate LASER marking on the microstructure of deposition

Figure 12(a) shows the microstructure for Laser-hybrid deposition at 1000X magnification and Figure 12 (b) shows the microstructure for GMAW-WAAM deposition at 1000X magnification

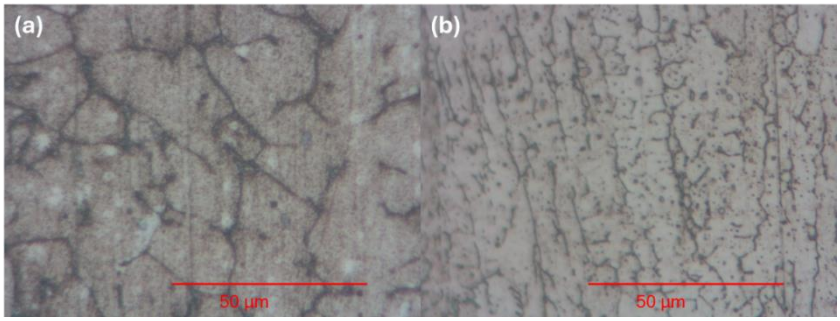

Fig 4.11 (a). Microstructure for Laser-hybrid deposition at 1000X magnification (b) Microstructure for GMAW-WAAM deposition at 1000X magnification

From Figure 4.11 (a) and (b) it can be inferred that by laser-hybrid deposition, the grain size of SS-304L is reduced. A possible reason for this could be that the laser marking process generates microstructural features on the substrate surface, which can serve as nucleation sites during deposition. This can result in a higher number of nucleation events and finer grains. These microstructural features created by the laser marking

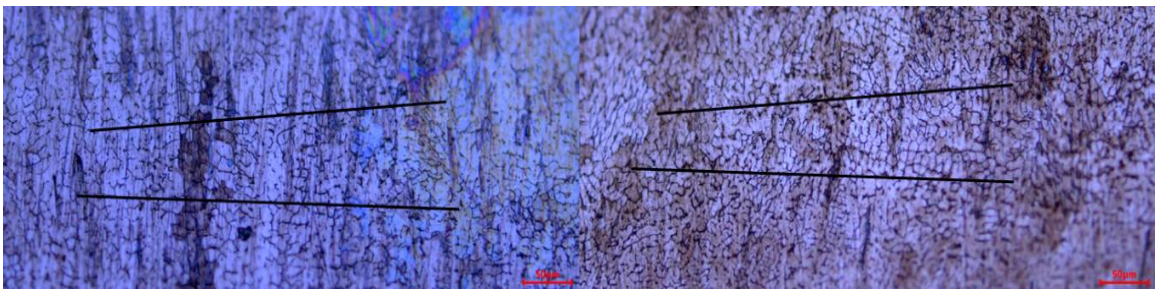

process may play a role in enhancing nucleation during deposition, ultimately leading to the formation of finer grains in the material.

Fig 4.12(a). Micrograph of GMAW-WAAM deposition (b) Micrograph of Laser-hybrid deposition

Figure 4.12(a) shows the micrograph for GMAW-WAAM deposition and Figure 4.12(b) shows the micrograph for Laser-hybrid deposition. Through the line-intercept method applied on these images, the grain size of both depositions was calculated and compared as shown in Table 4.9. The higher value of G indicates finer grains, depicting a reduction in grain size. It can be calculated from Table 4.9 that the grain size was reduced by 6.7%.

Table 4.9 Grain size of deposition by GMAW-WAAM and Laser-hybrid WAAM

Process	**GMAW-WAAM**	**Laser-hybrid WAAM**
Mean intercept length	0.0155	0.0106
Grain size number	15.323	16.42

4.2.2 Effect of substrate LASER marking on the hardness of deposition

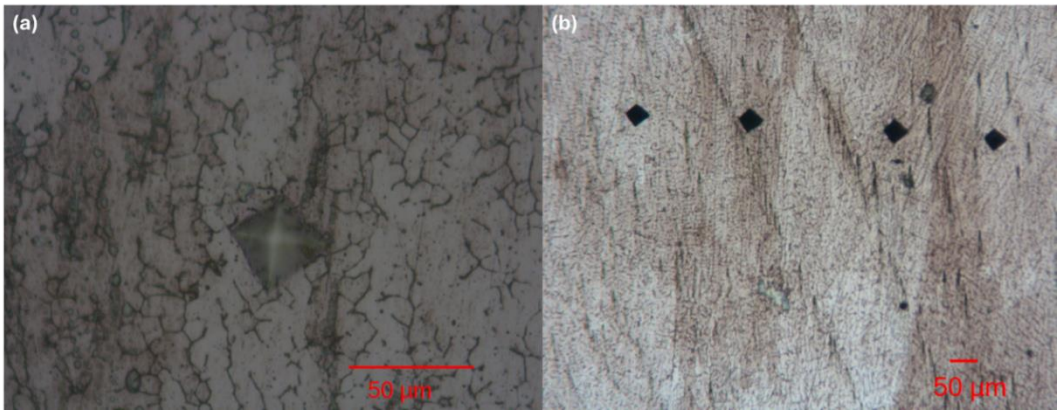

Fig 4.13(a). Indentation mark for deposition at 1000X magnification (b) Indentation mark for deposition at 200X magnification

The microhardness at 0.2 N load is determined at various positions (shown in Fig 4.9), using a Vickers microhardness tester (Econamet VH-1MDX) with a 10 s dwell period is performed. Indentation marks at different magnifications, 1000X and 200X respectively, can be seen from Fig 4.13 (a) and (b).

Table 4.10 Vickers Micro-Hardness for deposition at the optimum level of parameters

Deposition Technique	**Position for Vicker's Hardness Test**	**Value (HV)**
GMAW-WAAM	Bottom (1)	260.1
	Intermediate (2)	218.4
	Middle (3)	206.9
	Intermediate (4)	191.5
	Top (5)	201.6
LASER-Hybrid WAAM	Bottom (1)	285.4
	Intermediate (2)	230.6
	Middle (3)	219.3
	Intermediate (4)	216.9
	Top (5)	219.2

The Vickers hardness shows a decrease in value from the bottom to the top of the deposition, with a slight increase at the top layer due to higher cooling rate. This can be validated from Table 10. Moreover, the hardness value of laser-hybrid deposition is 8.6% more than the GMAW-WAAM deposition. This is due to the finer grain structure in laser-hybrid deposition. In comparison with the laser-hybrid deposition, it shows a better hardness value as compared to the GMAW-WAAM deposition for each subsequent layer.

4.3 Characterization of Deposited and Heat-treated NiTi Samples

After understanding thoroughly, the effect of WAAM process parameters on the deposition and the laser-hybrid WAAM, we went ahead with the optimization of NiTi deposition. It was done based on the uniformity of deposition and energy per unit length of the deposition, then annealing of the optimized NiTi deposition at 850 ºC with a heating rate of 10 ºC/min, holding time of 1 hour with furnace cooling was done. Both the annealed and the unannealed depositions were compared based on the microstructure, mechanical properties and transformation temperatures. A NiTi wire (50.9 at% Ni), of diameter 1.2 mm was deposited by GMAW-WAAM. The voltage and wire feed rate were varied based on a full factorial design of experiment and the single-layer deposition at each combination of parameters was done as shown in Figure 2.

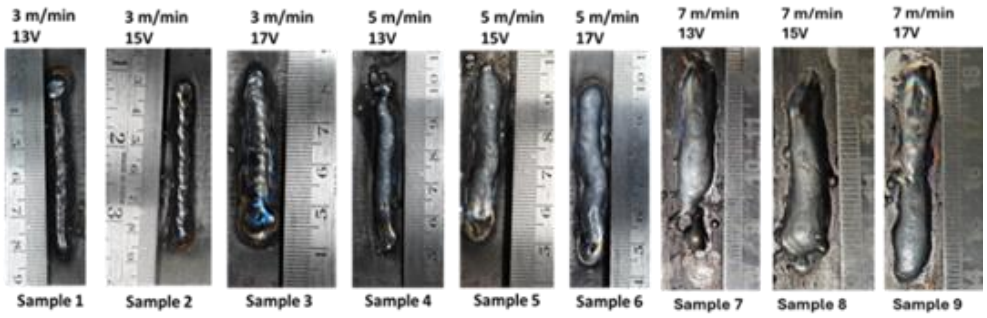

Fig. 4.14: Single track deposition of NiTi on a Ti substrate.

Table 4.11: Full factorial design for NiTi deposition

No.	Feed Rate,f (m/min)	Voltage (V)	Current (I)	Energy/length, E (kJ/m)	Argon flow Rate(L/min)	Response (Width) (mm)
1	**3**	**13**	52	13.52	**20**	**4.1**

2	3	15	63	18.9	20	4.2
3	3	17	70	23.8	20	5.7
4	5	13	89	13.88	20	5.2
5	5	15	91	16.38	20	6.7
6	5	17	98	19.99	20	7.1
7	7	13	92	10.25	20	12.2
8	7	15	102	13.11	20	13.4
9	7	17	110	16.03	20	13.7

For each combination of parameters, the energy per unit length is calculated and is shown in Table 4.11.

$$E = (V*I) / f \quad \text{---------- (4.4)}$$

Eq. 4.4 is used to calculate the energy per unit length of the deposition. Where E is energy per unit length (kJ/m), V is voltage (V), I is current (A), and f is scan speed (mm/s). The depositions no. (7 and 8) were not uniform. Therefore, to select the optimized deposition we went ahead with the remaining depositions. As NiTi characteristics are highly dependent on heat input, the deposition with lowest energy per unit length was selected for further analysis. The deposition with the lowest energy per unit length, is deposition no. 1.

The optimized deposition was cut using a wire-EDM and then annealed at 850 ºC in a Muffle furnace for a holding time of 1 hour and then furnace cooled. The samples were prepared using standard metallography techniques and then the microstructure was evaluated using a FESEM. The FESEM results at magnification of 500X and 1000X are shown in Figure 4.15.

The SEM results show that the microstructure has one bright phase and one dark phase (Figure 4.15). These phases could be the different NiTi phases present in the matrix. The bright phase is NiTi and the dark phase is Ti2Ni, which is validated from EDS and

XRD results. The findings demonstrate that the annealing causes the agglomeration of NiTi grains and an increase in their size. This phenomenon may be attributed to grain boundary migration during furnace cooling, resulting in the coalescence of smaller grains into larger agglomerates. The grain size was calculated from the SEM images using the ImageJ software and the grain size was observed to increase from 9.04 µm in the as-deposited state to 12.81 µm following annealing.

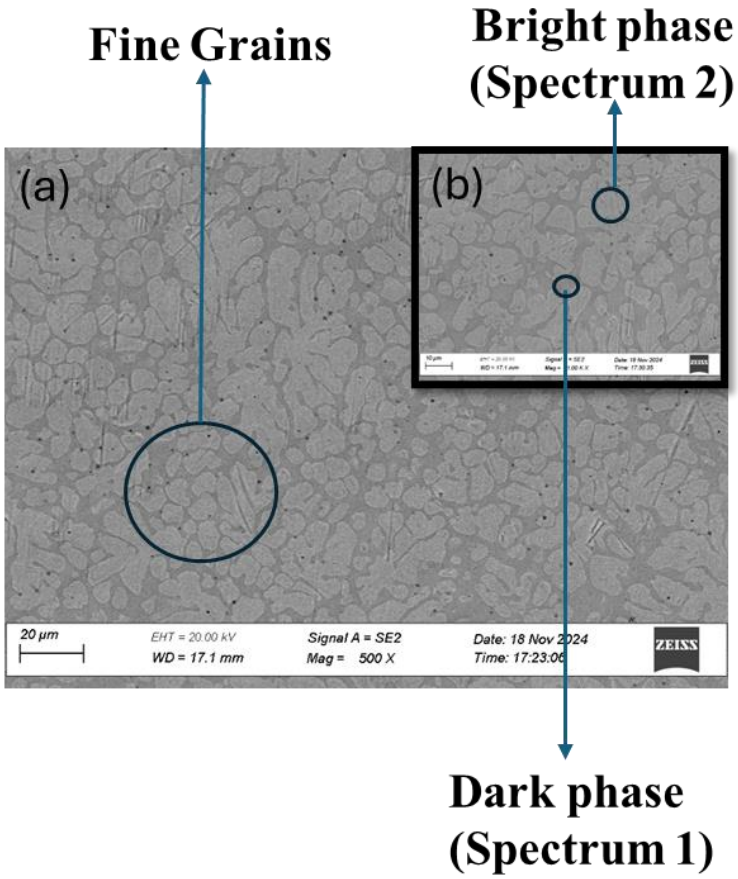

Fig. 4.15 (a) Microstructure of as deposited NiTi at 500X Magnification (b) Microstructure of as deposited NiTi at 1000X Magnification.

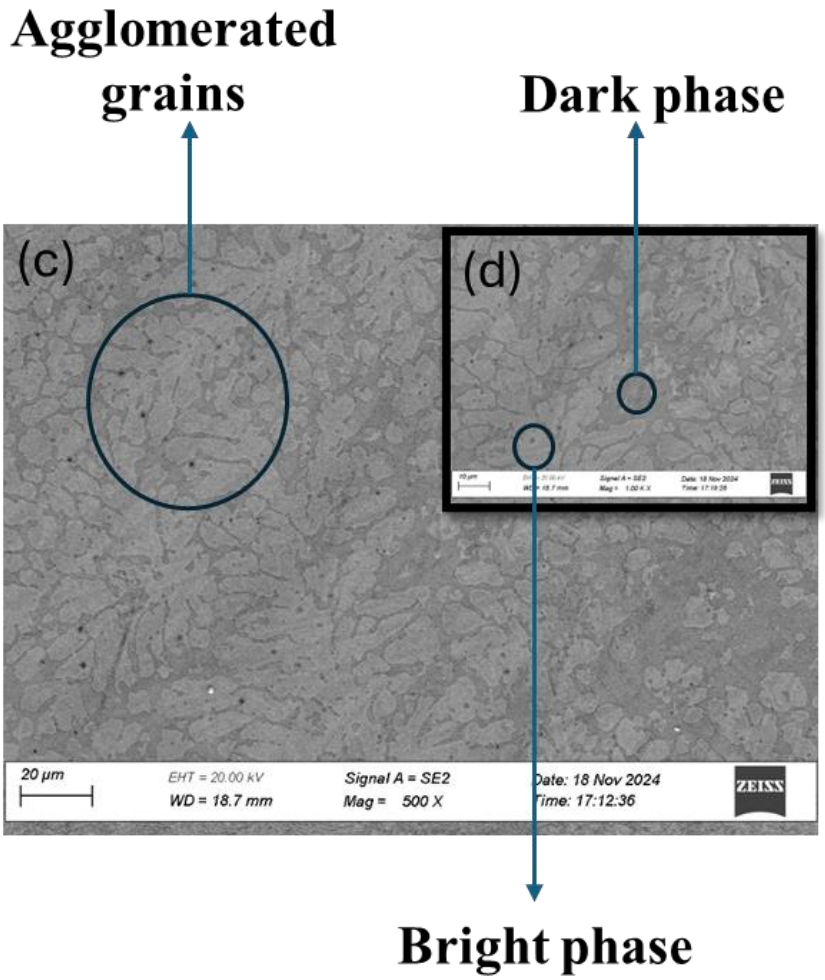

Fig. 4.15 (c) Microstructure of annealed NiTi at 500X Magnification (d) Microstructure of annealed NiTi at 1000X Magnification and annealed NiTi

The EDS mapping was done through SEM+EDS setup (ZEISS Gemini SEM 360). Figure (4.18,4.19) shows the distribution of Ni and Ti throughout the cross section for both as deposited and annealed samples. It can be concluded from Figure (4.18,4.19), that the distribution of Ni and Ti is uniform throughout the cross section of the deposition and the difference in composition of Ni and Ti in two visible phases indicates the formation of NiTi and Ti2Ni, which is in accordance to the phase diagram of NiTi and the point EDS results as shown in Figure (4.16,4.17). From Figure 4.16, it

can be observed that the percentage of Ti is around twice the Ni percentage and from Figure 4.17, it can be observed that their percentages are almost equal. Figure 4.19 indicates some carbon deposits in the annealed samples, this is because the annealing was performed in open conditions.

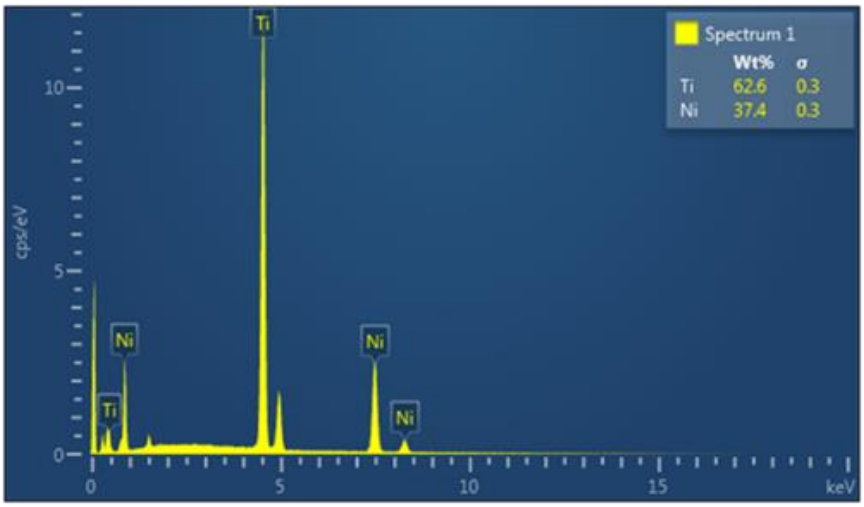

Fig. 4.16 EDS result for spectrum 1 as shown in fig. 4.15 (b)

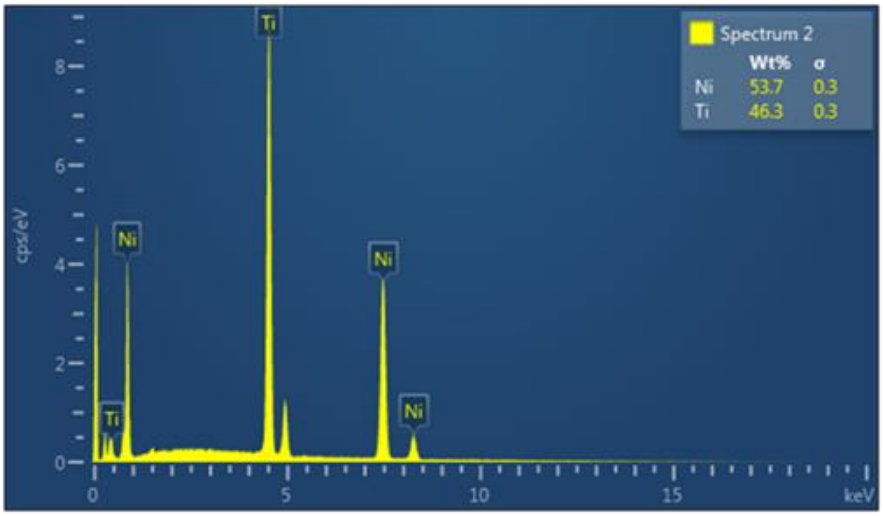

Fig. 4.17 EDS result for spectrum 2 as shown in fig. 4.15 (b)

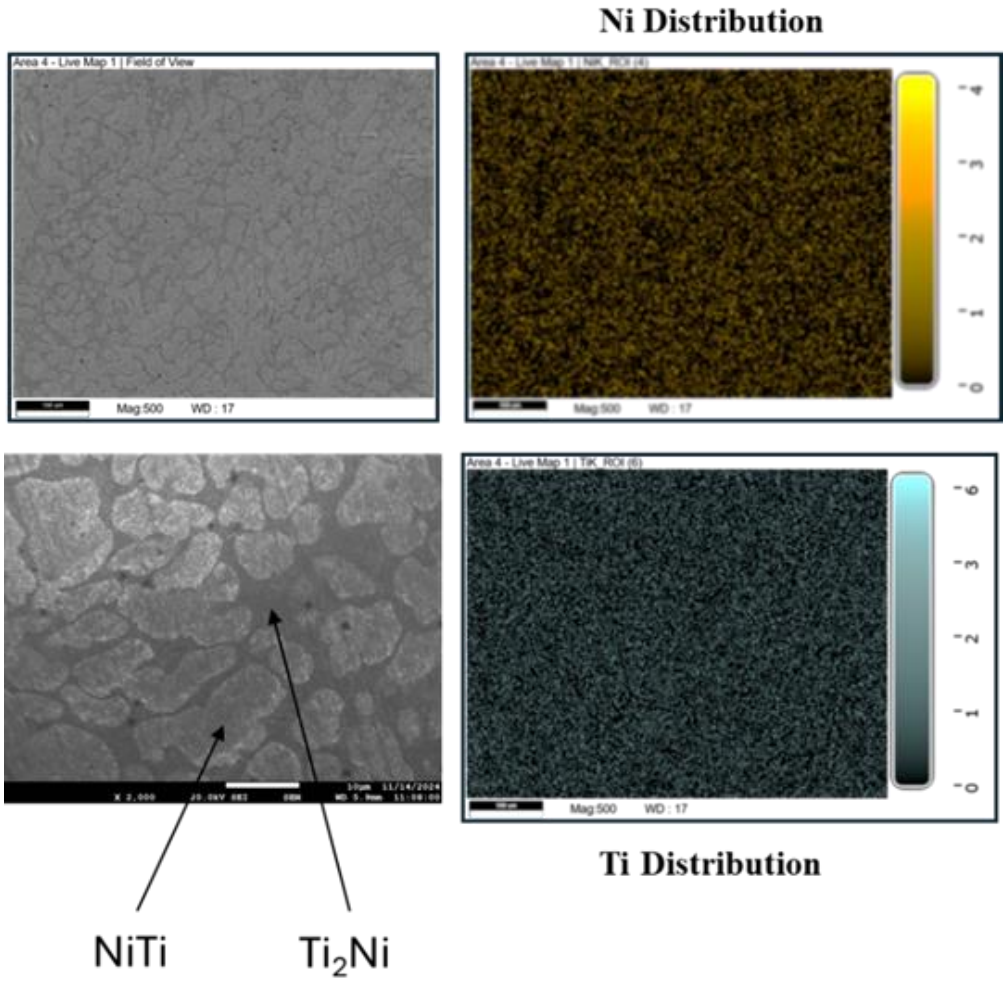

Fig. 4.18 EDS Mapping for as-deposited sample.

The XRD for as deposited as well as annealed samples was also done through PANalytical Empyrean, XRD setup and its analysis was done using the Xpert HighScore software. The findings of XRD are shown in Figure 4.20, which confirmed the formation of NiTi and Ti_2Ni phases, validating the SEM-EDS results. Also, the annealed sample displayed the reduction in Ti_2Ni peaks, which decreased from 4 in number in the as deposited sample to only 2 in number in the annealed sample. The transformation of Ti_2Ni into NiTi could be a reason for the disappearance of Ti_2Ni peaks. The reduction in Ti_2Ni peaks can lead to an increase in the ductility of the

annealed samples. The DSC results are shown in Figure 4.21 which depicts that the average transformation temperature of the wire is 74.5 ºC, which decreases to 70.7 ºC for as-deposited sample, which further decreased to 58.6 ºC, for the annealed sample. The decrease in

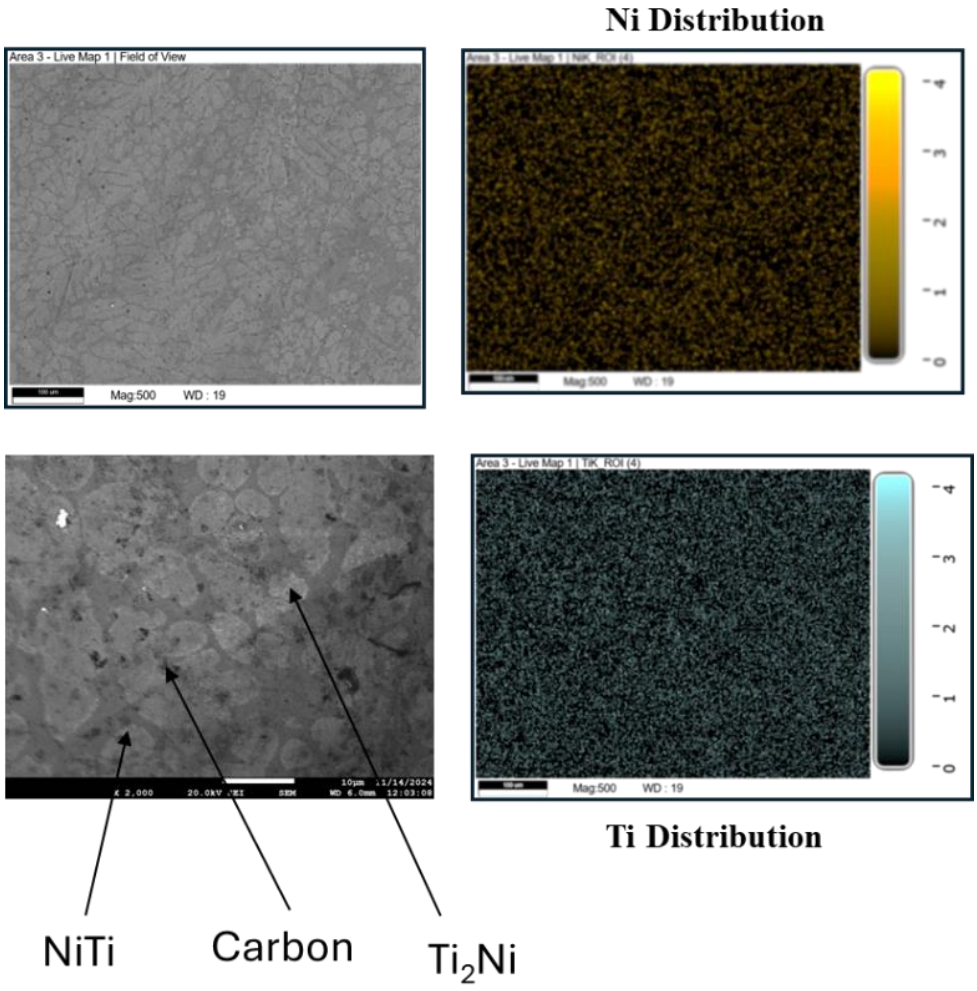

Fig. 4.19 EDS Mapping for annealed sample.

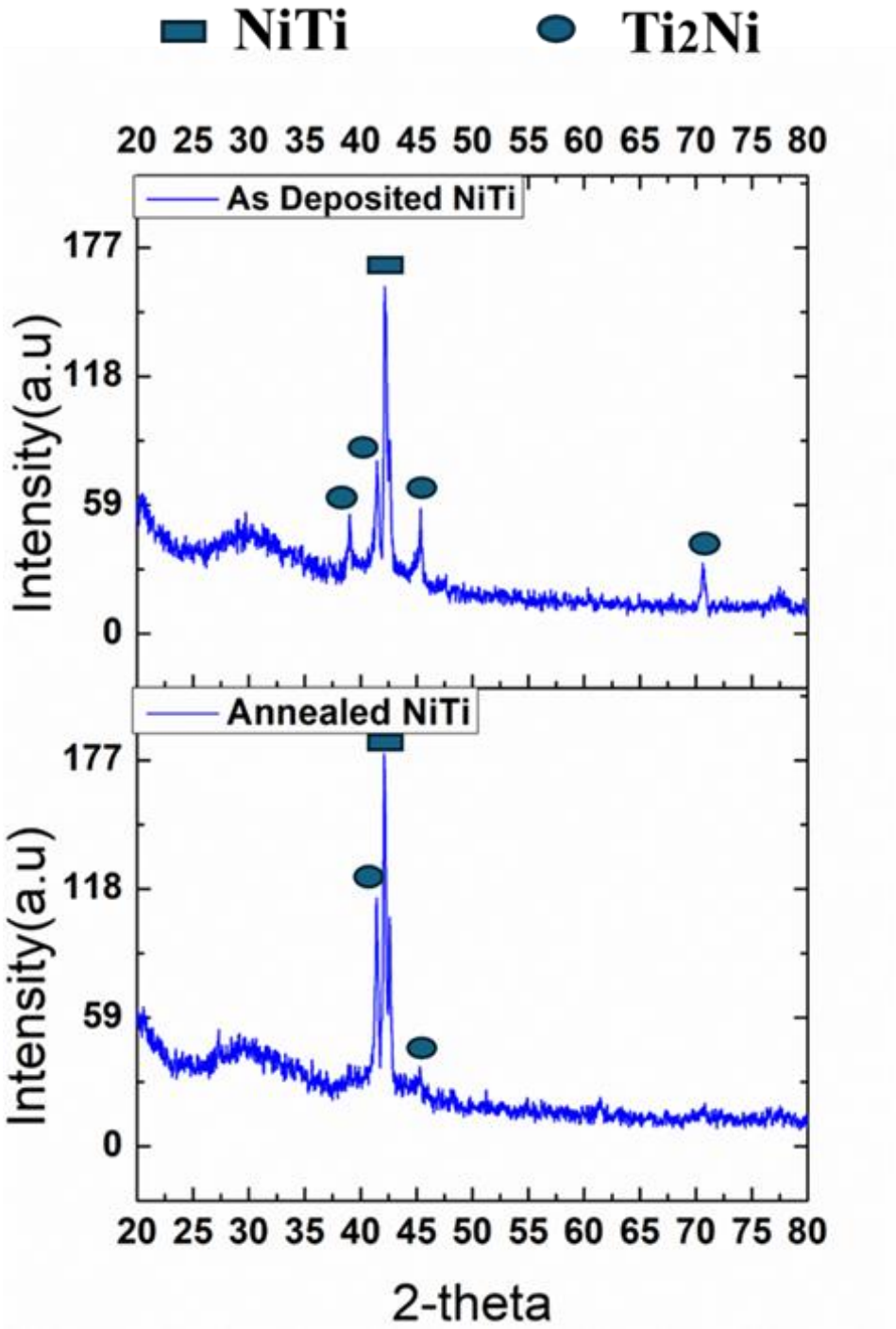

Fig. 4.20 XRD results for as deposited NiTi and annealed NiTi

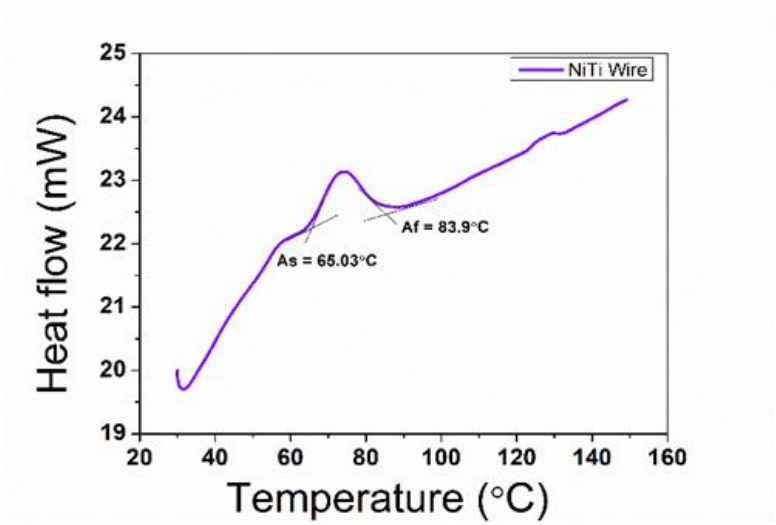

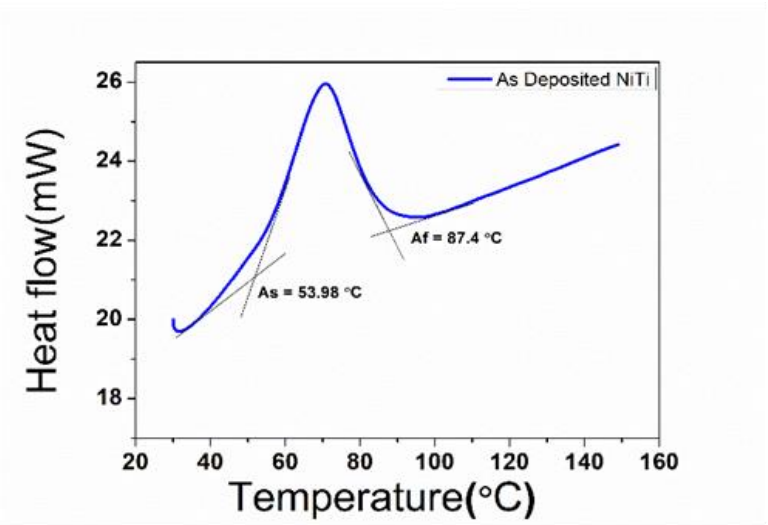

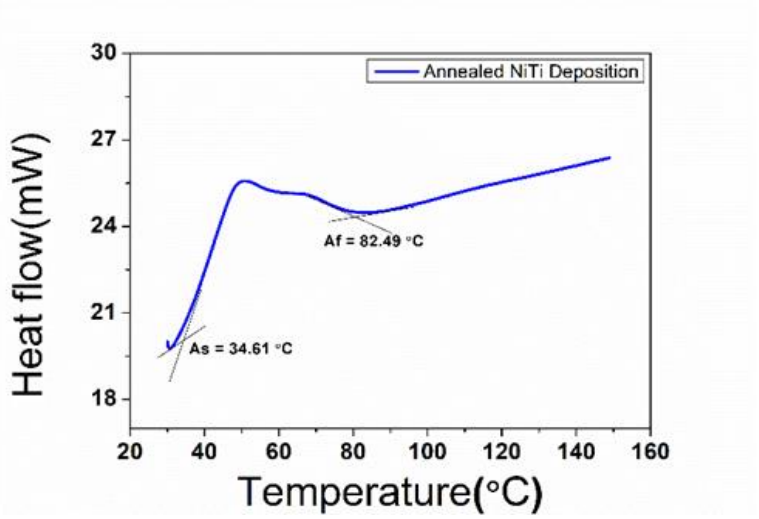

Fig. 4.21 DSC results for (a) wire, (b)as deposited NiTi and (c)annealed NiTi(As = Austenite start temp., Af = Austenite finish temp.)

and Ti-rich interdendritic zones, this creates local variations in Ni:Ti ratios, slightly increasing the effective Ni content in the matrix compared to the wire, which leads to the reduction of transformation temperature.

The micro hardness test was performed using Vicker's microhardness tester (Econamet VH-1MDX), with a 1 kg load and a dwell time of 10s. The micro hardness test was done for both as deposited samples and annealed samples at 5 different locations separated by 1mm distance. The micro hardness comparison (Figure 4.22) between the as deposited sample and the annealed sample shows a decrease in the average hardness from 337.3 Hv to 302.54 Hv, indicating stress relaxation. The reduction in hardness could be due to the increase in grain size after annealing and the reduction in Ti_2Ni phase as depicted through XRD results.

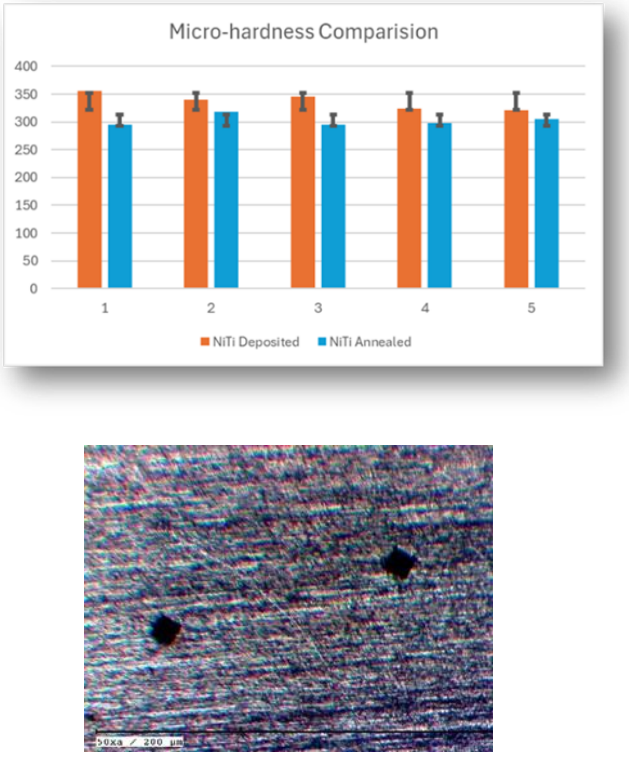

Fig. 4.22 (a)Micro-hardness comparison for as deposited NiTi and annealed NiTi and (b)Indentation Marks on the samples.

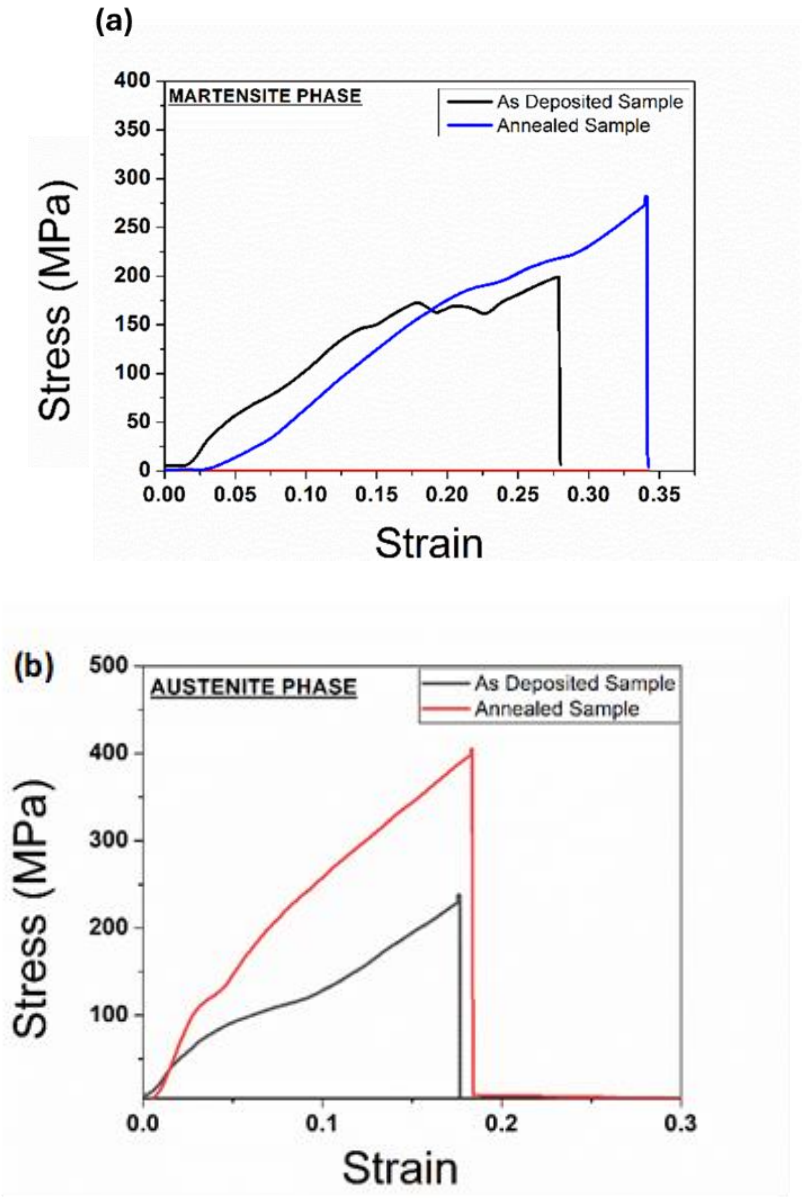

Fig. 4.23 Tensile test for (a) Martensite phase and (b) Austenite phase.

The samples were tested for tensile testing using a universal tensile testing machine, revealing an increase in ultimate tensile strength and strain, indicating enhanced ductility consistent with XRD and micro-hardness findings. Tensile tests were conducted at room temperature in the martensite phase and at 120 ºC in the austenite phase, with results depicted in Figure 4.23. The ultimate tensile strength rose from 199.13 MPa to 286.53 MPa in the austenite phase and from 237.53 MPa to 404.8 MPa

in the martensite phase, suggesting an improvement in properties, the improvement in properties could be attributed to the reduction in residual stress and increase in NiTi phase.

4.4 Effect of Process Parameters on composition and transformation temperatures.

4.4.1 Multilayer Deposition

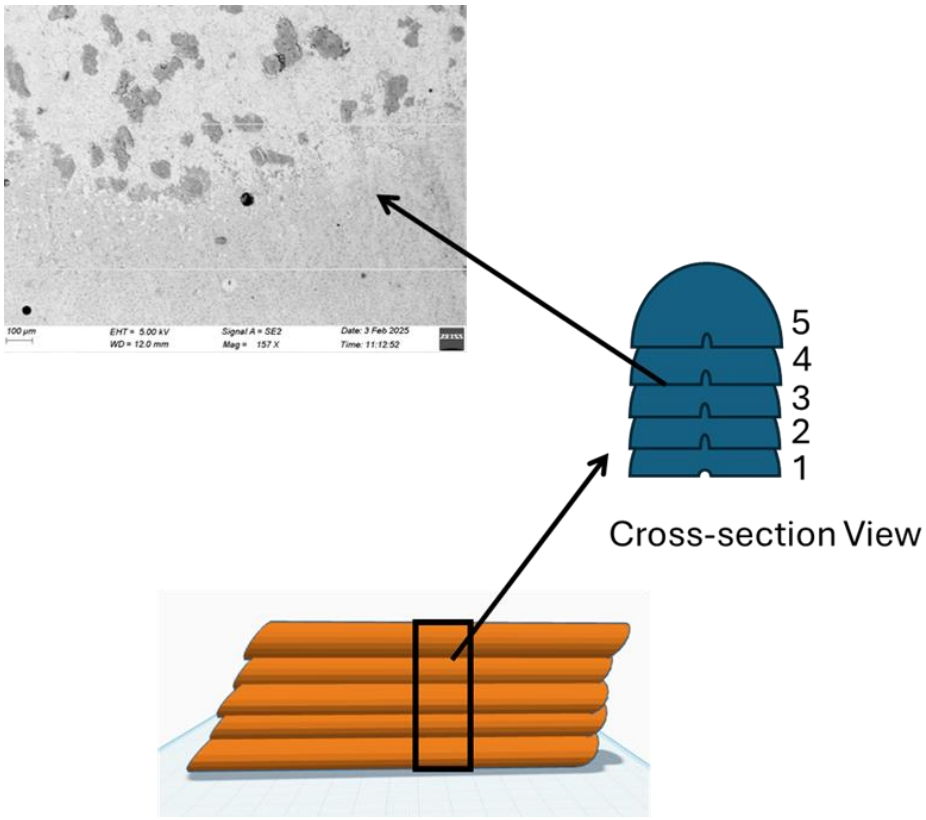

Fig.4.24 Multilayer deposition schematic

A NiTi wire of 1.2mm diameter was used for a 5-layer deposition on a Ti substrate. The deposition was done on a voltage of 13V and wire-feed rate of 3m/min. The schematic of the deposition is shown in Figure. 4.24. EDS at each layer was done and is shown in Figure 4.25.

Bottom layer

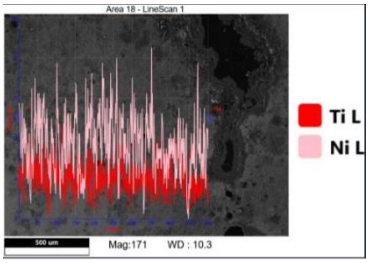

Element	Weight %	MDL	Atomic %	Error %	Net Int.	R	A	F
Ti L	78.9	1.4	82.1	9.7	78.2	0.8222	0.2120	1.0000
Ni L	21.1	0.82	17.9	10.4	69.4	0.8392	0.1796	1.0000

Layer 2

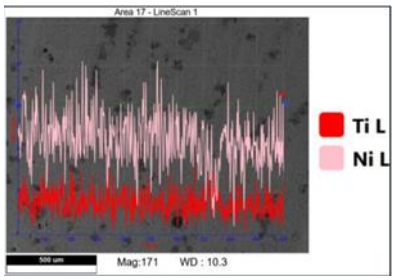

Element	Weight %	MDL	Atomic %	Error %	Net Int.	R	A	F
Ti L	64.9	1.86	69.4	10.1	51.6	0.8169	0.1976	1.0000
Ni L	35.1	0.55	30.6	10.1	111.0	0.8341	0.2004	1.0000

Layer 3

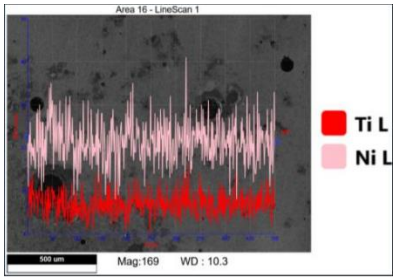

Element	Weight %	MDL	Atomic %	Error %	Net Int.	R	A	F
Ti L	62.1	1.93	66.7	10.1	45.1	0.8159	0.1952	1.0000
Ni L	37.9	0.61	33.3	10.0	113.4	0.8331	0.2051	1.0000

Layer 4

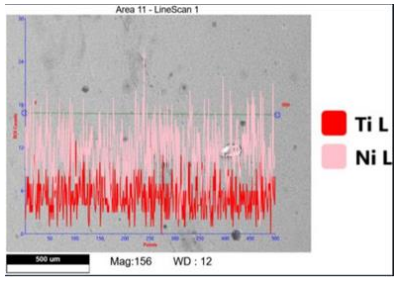

Element	Weight %	MDL	Atomic %	Error %	Net Int.	R	A	F
Ti L	58.3	8.17	63.1	9.2	14.3	0.8367	0.6502	1.0000
Ni L	41.7	3.9	36.9	8.8	35.6	0.8604	0.7092	1.0000

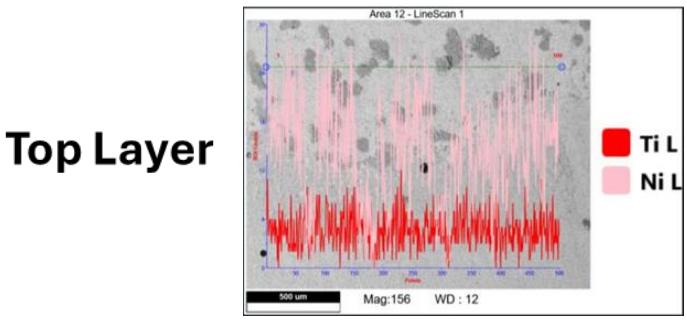

Element	Weight %	MDL	Atomic %	Error %	Net Int.	R	A	F
Ti L	44.8	8.48	49.9	9.4	10.6	0.8319	0.6520	1.0000
Ni L	55.2	4.29	50.1	8.4	46.7	0.8559	0.7319	1.0000

Fig. 4.25 EDS results for each layer in multilayer deposition

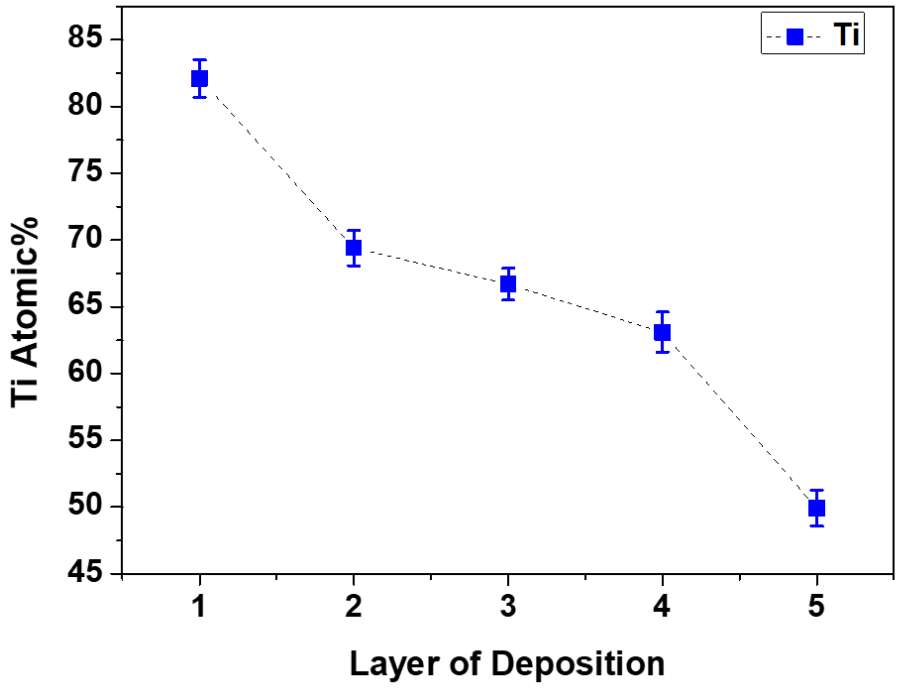

Fig. 4.26 Overall trend of Ti concentration

The EDS result from Figure 4.26 clearly shows that there is a reduction in the percentage of Ti in the deposition as we move upwards along the cross section of deposition. The reason for this composition change is the use of Ti plate as a substrate to deposit the NiTi bead, which leads to the diffusion of Ti in the NiTi deposition along the height of deposition.

4.1.2 Multilayer deposition at different energy/length

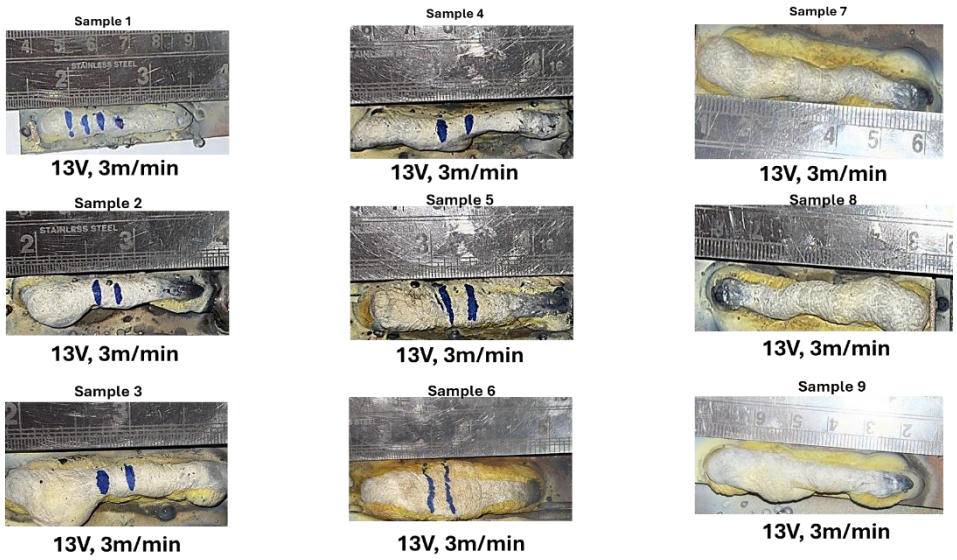

Fig. 4.27 Multilayer deposition of NiTi at different parameters shown in Table 4.12

A six- layer deposition of NiTi wire was done based on different varied parameters using full factorial design. The top-view of the deposition is shown in Figure 4.27 and the energy/length for different parameters is tabulated in Table 4.12.

Table 4.12 Energy/length of NiTi deposition at different WAAM parameters

No.	Feed Rate(m/min)	Voltage (Volts)	Current (Ampere)	Energy/length (kJ/m)
1	3	13	35	9.1
2	4	13	45	8.77
3	5	13	60	9.36
4	3	14	35	9.8
5	4	14	45	9.45

6	5	14	55	9.24
7	3	15	35	10.5
8	4	15	45	10.12
9	5	15	55	9.9

After cutting the samples using wire-EDM, homogenization of all the 9 samples was performed at 1000 ºC for 2 hours. Then, the EDS analysis of all the samples was performed for the middle portion of the crossection. The EDS results are shown in Figure 4.28.

Sample 1

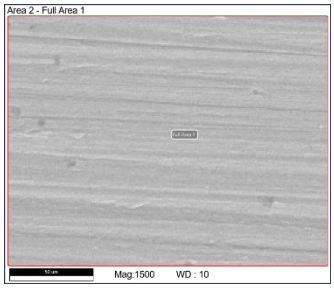

eZAF Quant Result - Analysis Uncertainty: 2.89 %

Element	Weight %	MDL	Atomic %	Error %	Net Int.	R	A	F
Ti K	45.9	0.4	51.0	2.7	660.0	0.8846	0.9137	1.0522
Ni K	54.1	0.53	49.0	3.0	341.7	0.9148	0.9374	1.0361

Sample 2

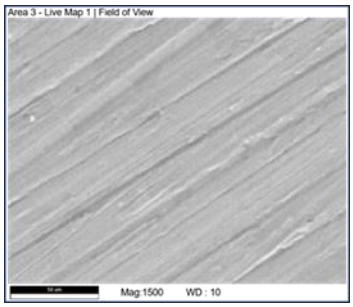

eZAF Quant Result - Analysis Uncertainty: 2.89 %

Element	Weight %	MDL	Atomic %	Error %	Net Int.	R	A	F
Ti K	45.5	0.43	50.5	2.8	657.7	0.8844	0.9133	1.0527
Ni K	54.5	0.72	49.5	3.0	346.7	0.9147	0.9377	1.0361

Sample 3

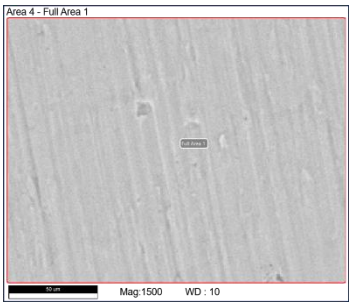

eZAF Quant Result - Analysis Uncertainty: 4.04 %

Element	Weight %	MDL	Atomic %	Error %	Net Int.	R	A	F
Ti K	47.8	1.39	52.9	3.3	689.2	0.8852	0.9144	1.0498
Ni K	52.2	1.09	47.1	4.1	329.9	0.9153	0.9357	1.0364

Sample 4

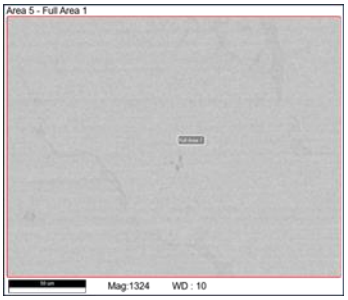

eZAF Quant Result - Analysis Uncertainty: 3.48 %

Element	Weight %	MDL	Atomic %	Error %	Net Int.	R	A	F
Ti K	47.2	0.42	52.3	2.7	670.9	0.8850	0.9143	1.0506
Ni K	52.8	0.51	47.7	3.0	329.3	0.9151	0.9363	1.0363

Sample 5

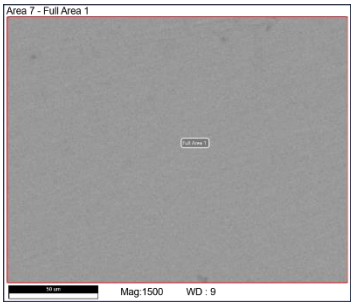

eZAF Quant Result - Analysis Uncertainty: 3.20 %

Element	Weight %	MDL	Atomic %	Error %	Net Int.	R	A	F
Ti K	45.8	0.48	50.8	2.9	492.7	0.8845	0.9119	1.0524
Ni K	54.2	0.59	49.2	3.2	256.8	0.9147	0.9363	1.0361

Sample 6

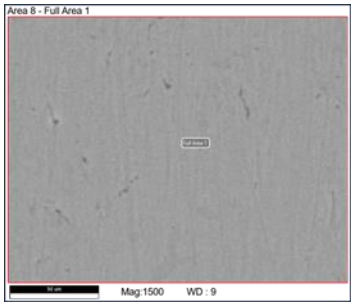

eZAF Quant Result - Analysis Uncertainty: 3.34 %

Element	Weight %	MDL	Atomic %	Error %	Net Int.	R	A	F
Ti K	46.0	0.67	51.1	2.9	499.4	0.8846	0.9122	1.0521
Ni K	54.0	0.67	48.9	3.2	257.7	0.9148	0.9362	1.0361

Sample 7

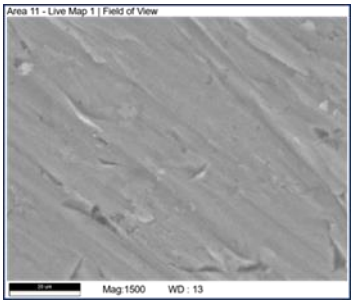

eZAF Quant Result - Analysis Uncertainty: 6.61 %

Element	Weight %	MDL	Atomic %	Error %	Net Int.	R	A	F
Ti K	48.9	0.39	54.0	2.9	937.4	0.8855	0.9185	1.0486
Ni K	51.1	0.76	46.0	3.4	429.9	0.9155	0.9376	1.0365

Sample 8

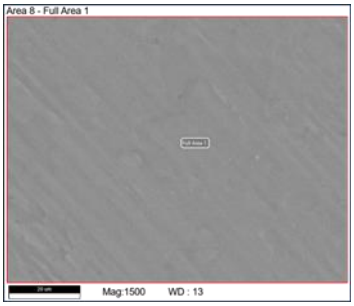

eZAF Quant Result - Analysis Uncertainty: 3.40 %

Element	Weight %	MDL	Atomic %	Error %	Net Int.	R	A	F
Ti K	48.0	0.53	53.1	2.7	934.1	0.8852	0.9179	1.0497
Ni K	52.0	0.56	46.9	3.1	444.3	0.9153	0.9382	1.0364

Sample 9

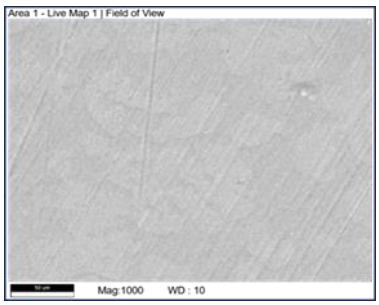

eZAF Quant Result - Analysis Uncertainty: 2.89 %

Element	Weight %	MDL	Atomic %	Error %	Net Int.	R	A	F
Ti K	45.6	0.37	50.7	2.8	649.1	0.8845	0.9134	1.0525
Ni K	54.4	0.56	49.3	3.0	339.9	0.9147	0.9375	1.0361

Fig. 4.28 EDS results for all 9 depositions tabulated in Table 4.12

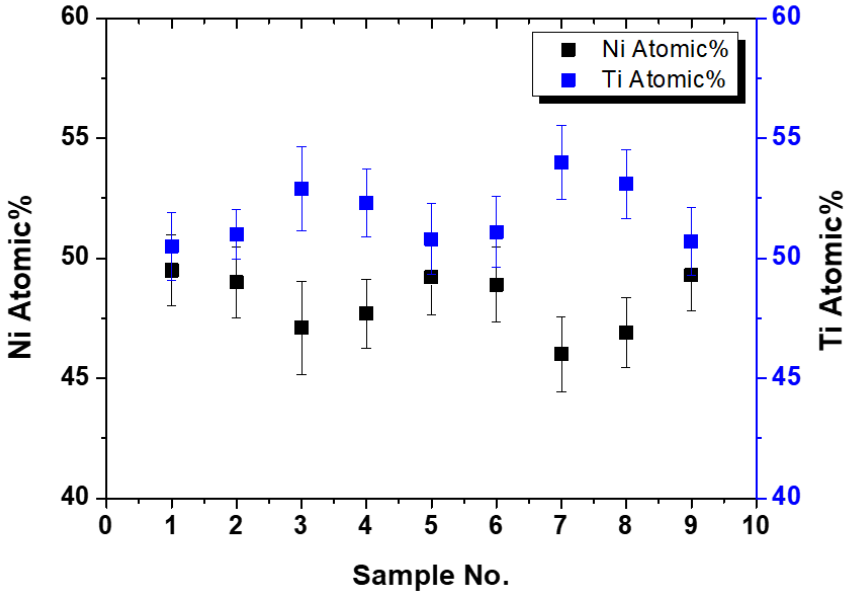

Fig. 4.29 EDS results for variation of atomic% of Ni and Ti for all 9 deposited samples

The EDS results for all the 9 depositions are shown in Figure 4.28 and the atomic percentage of Ni and Ti is shown through a scatter plot shown in Figure 4.29. The EDS results for NiTi deposition at different parameters suggest that, more the energy density more the evaporation of Ni takes place. The possible reason for this could be due to the low melting point of Ni as compared to Ti.

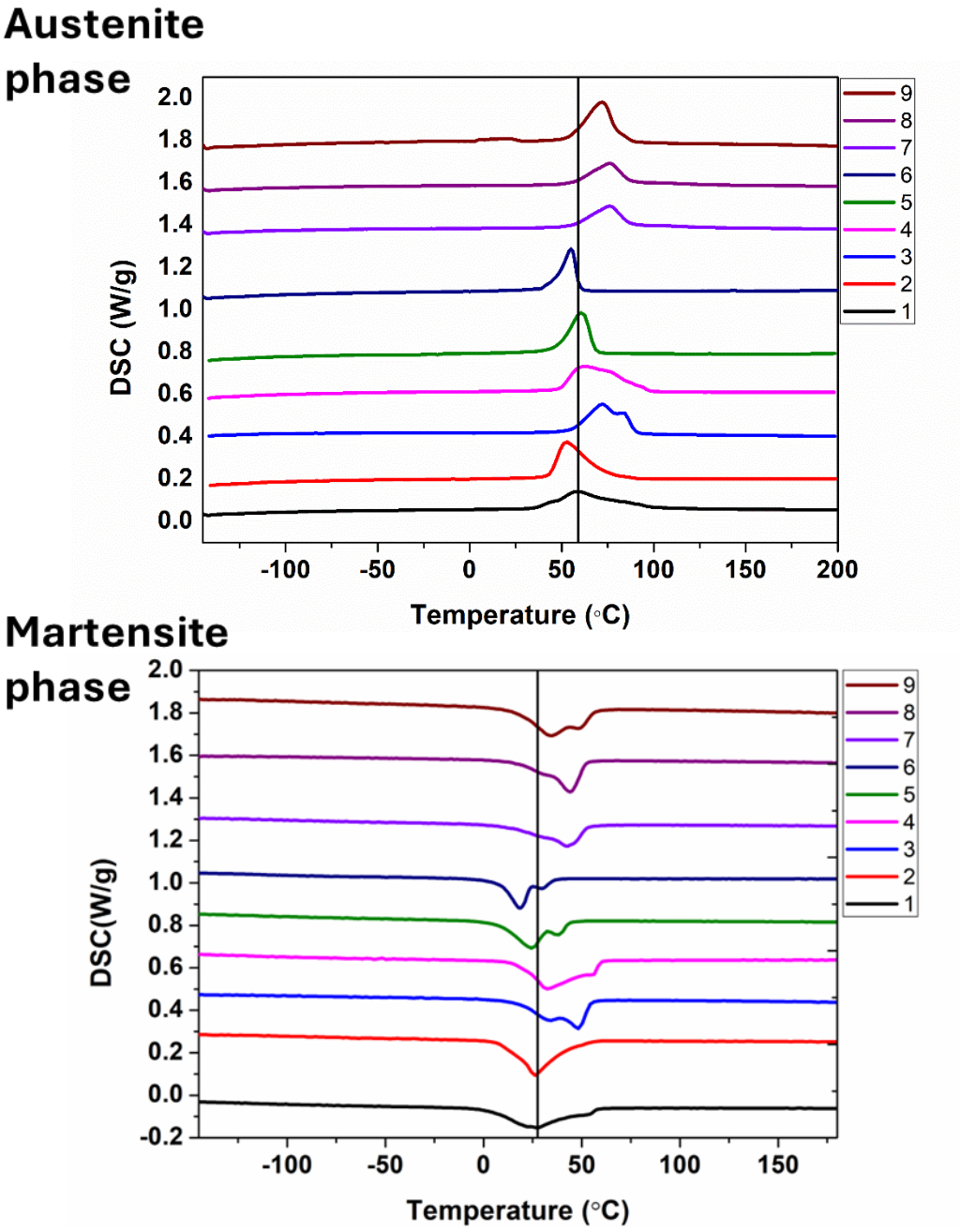

Fig. 4.30 DSC results for variation for all 9 deposited samples

From Figure 4.30, the DSC results for the 9 samples showed a relation of transformation temperature with different energy/length. Higher energy/ length showed a higher transformation temperature, whereas a lower energy/length showed a lower transformation temperature. The possible reason for this could be the Ni

evaporation due to higher energy/length, which makes the matrix Ti rich causing the transformation temperature to increase. The transformation temperature along with the Ni atomic% is tabulated in Table 4.13.

Table 4.13 Transformation temperature of NiTi deposition at different WAAM parameters

Sample	Average austenitic transformation temp.	Average martensitic transformation temp.	Ni Atomic%
1	58.55	27.58	49
2	52.57	26.24	49.5
3	76.5	41.46	47.1
4	65.95	34.95	47.7
5	61.82	24.50	49.2
6	54.02	18	48.9
7	76.9	43.2	46
8	77.4	44.9	46.9
9	72.35	41.05	49.3

To further increase the transformation temperature, heat treatment was explored, in which solutionizing at 1000 ºC, followed by aging at 450 ºC was performed for 2 hours. The DSC results are shown in Figure 4.31 and 4.32 for austenitic and martensitic transformations respectively.

4.1.3 Effect of heat treatment on transformation temperature.

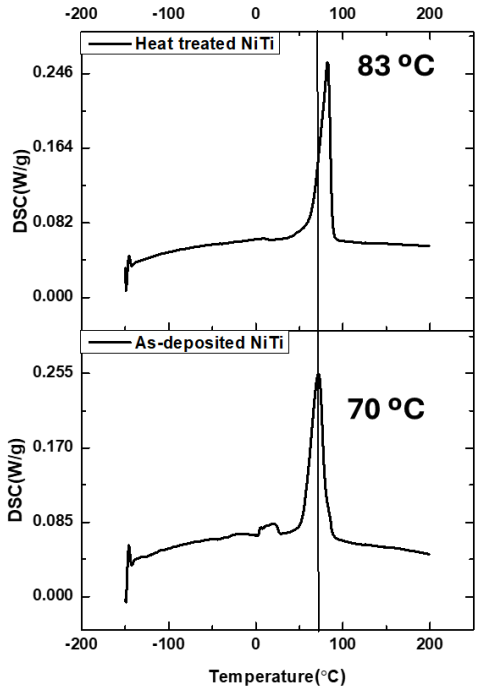

Fig.4.31 Comparison of austenitic transformation between as deposited and heat-treated sample

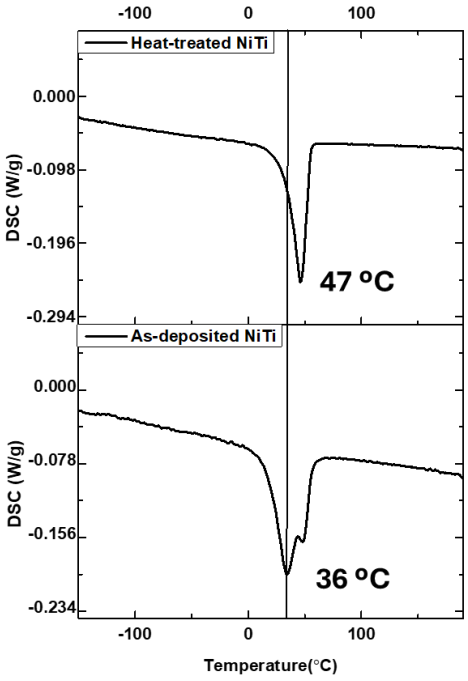

Fig.4.32 Comparison of martensitic transformation between as deposited and heat-treated sample

From Figure 4.31, 4.32, it can be seen that after heat treatment there is a increase in the transformation temperature in both the phases. The possible reason for this could be the precipitation of Ni-rich phases (like Ni_4Ti_3) during aging, which causes Ni depletion in the matrix. Since Ni-rich compositions lower the transformation temperature, reducing Ni content causes the temperature to rise.

4.4 Effect of Cu Addition on Properties

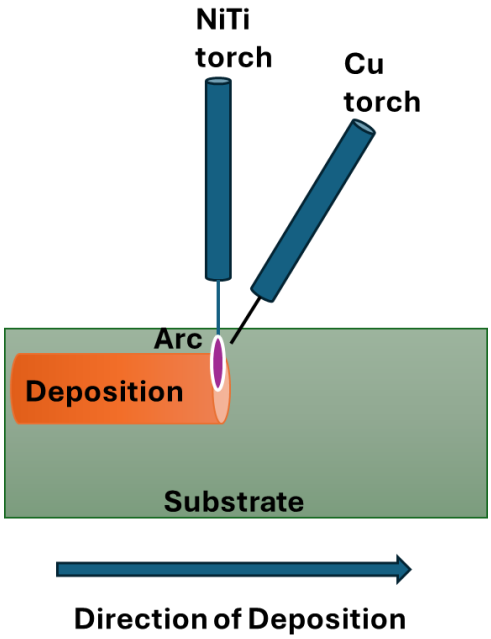

Fig.4.33 Schematic of Cu inclusion in NiTi

A Cu (99.9 atomic%) wire with a diameter of 1.2mm is used for Cu inclusion in NiTi deposition. The Cu is fused directly into the arc generated by the NiTi deposition and hence fused in the NiTi deposition. The schematic for Cu inclusion is shown in Figure 4.33. The DSC results for different NiTiCu deposition with varying Cu percentage is shown in Figure 4.34, 4.35 depicting austenite and martensite phase respectuively.

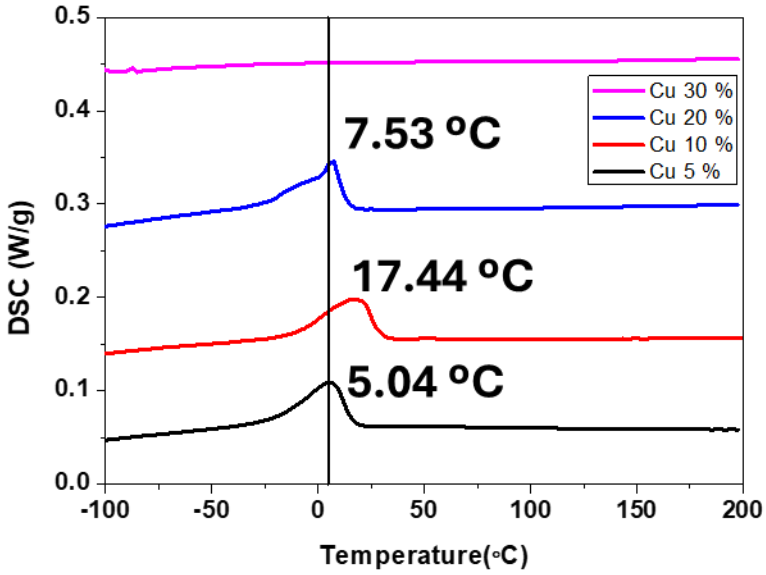

Fig.4.34 DSC of NiTiCu samples with varying Cu% while heating

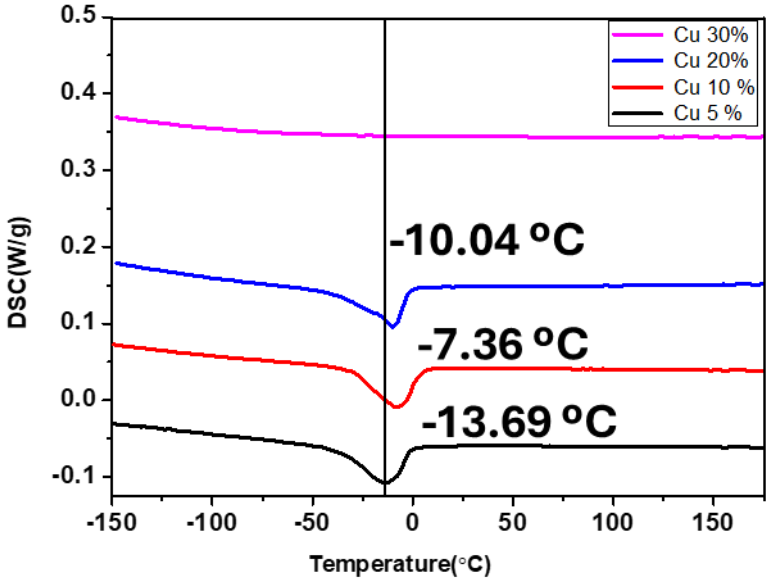

Fig.4.35 DSC of NiTiCu samples with varying Cu% while cooling

From Fig. 4.34, 4.35 there is a increase in transformation temperatures as the percentage of Cu increases from 5% to 10%, but there is a decrease in transformation temperatures as the Cu increases from 105 to 20% in the deposition. Also at 30% Cu, the shape memory diminishes and is shown from the DSC results. The possible reasons

to this trend could be : The increase in transformation temperature from 5% to 10% Cu is due to Cu substituting Ni, which stabilizes the martensite phase and sharpens transformations. Beyond 10% to 20% Cu, transformation temperatures drop due to the formation of Cu-rich secondary phases and a shift in transformation mechanism. At 30% Cu, the shape memory effect diminishes as brittle intermetallic form, disrupting the NiTi matrix and suppressing reversible transformation.

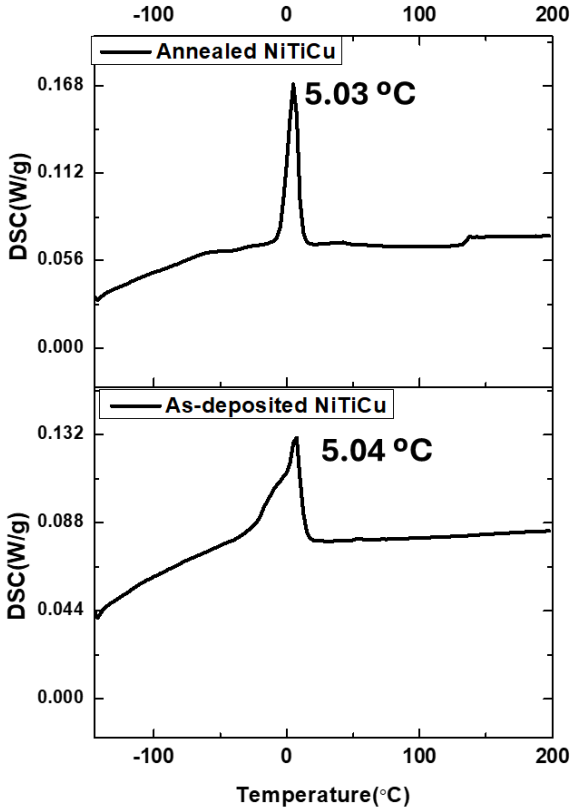

Fig.4.36 Effect of annealing on NiTiCu alloy

Annealing the $NiTiCu_x$ at 1000 ºC shows a sharper DSC peak the possible reason to this could be due to improved homogenization of the alloy and relief of internal stresses. At this high temperature, elemental diffusion is enhanced, reducing compositional inhomogeneities and dissolving secondary phases, which creates a more uniform matrix.

4.5 Training and Actuation Performance

4.5.1 Static Simulation Results

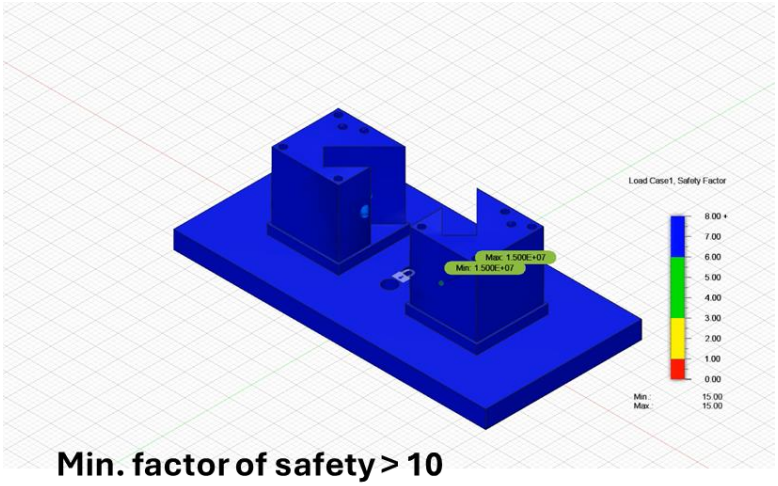

Min. factor of safety > 10

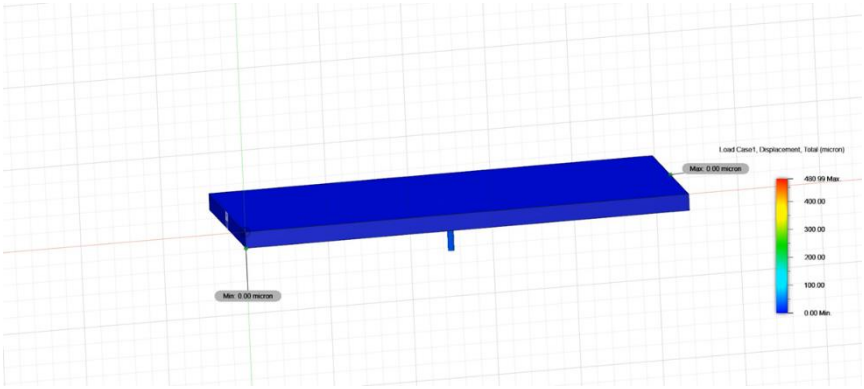

Max. Displacement = 0.48 mm

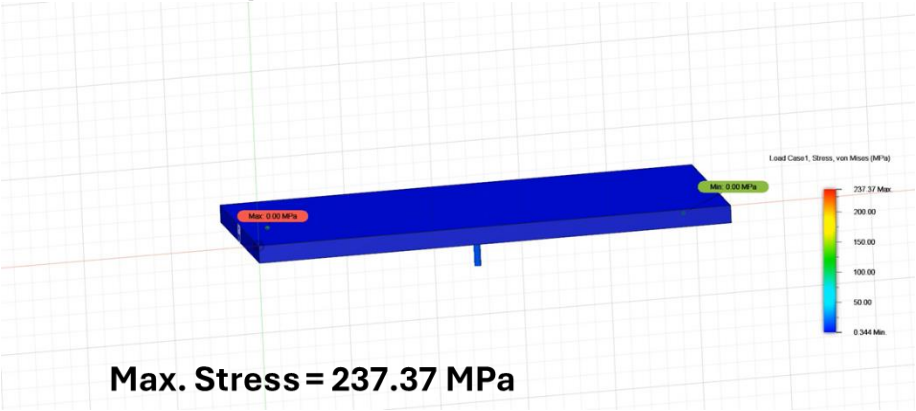

Max. Stress = 237.37 MPa

Fig.4.37 Simulation results for sheet produced from optimized NiTi deposition

The mechanical properties of the NiTi were calculated through testing and are tabulated in Table 4.14.

Table 4.14 Transformation temperature of NiTi deposition at different WAAM

E (annealed, martensite)	882.35 MPa
Density	5.5 * 10^ (-3) g/cm^3
Poisson's Ratio	0.33

The static simulation was done on Autodesk Fusion 360 by applying a static load of 40N and the max. stress generated was well below the safe limit and the max. displacement was 0.48 mm. Hence, the sheet produced can be used under a load of 40 N.

4.5.2 Training of samples

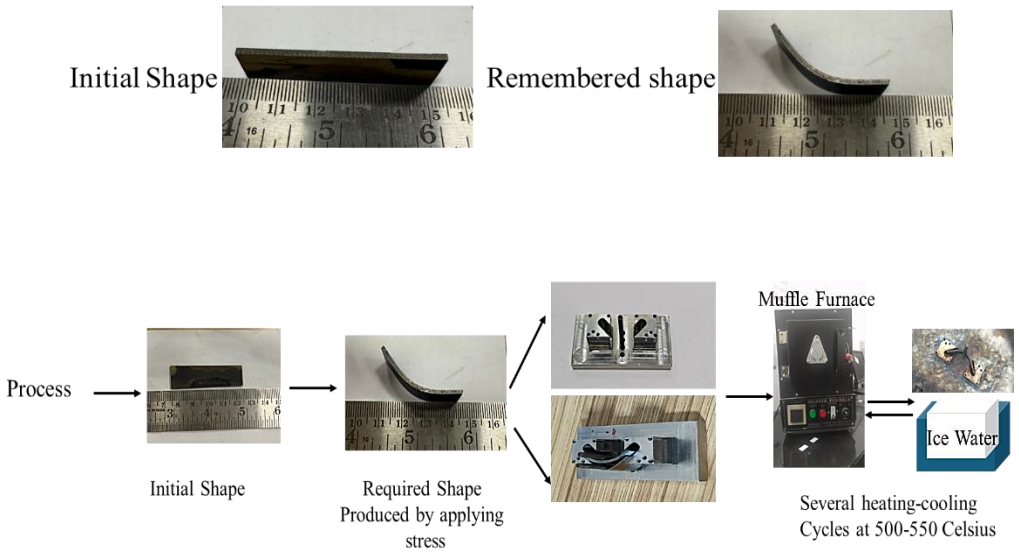

Fig. 4.38 Training/Shape-Setting of SMA Clamp

The sheet cut using wire-EDM was trained for actuating 90º and the training process is depicted in Figure 4.38

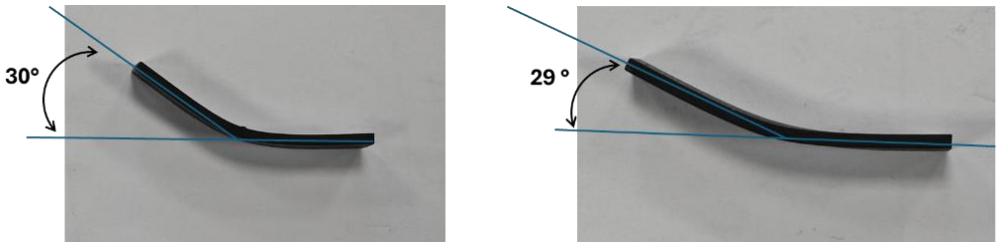

Fig. 4.39 Strain Recovery Calculation

Table 4.15 Strain Recovery after actuation

Radius of curvature, R	40.27mm
Thickness of plate, t	1.5mm
Strain %	(t/2R) * 100=1.86%
Strain Recovery %	96.7%

The samples were trained for 30º and showed a recovery on heating to 29º, hence showing a 96.7% recovery for the first cycle.

5.1 CONCLUSION

- Based on the screening design, it was found that Argon flow rate does not affect the geometry of the deposition.
- Based on the full factorial design for deposition of 10 layers and further using ANOVA, the aspect ratio was found to decrease with the increase in voltage and increase then decrease with the increase of wire feed rate.
- The results show that width is increasing with the increase in wire feed rate, and it is not affected much by voltage.
- The results show that height is decreasing with the increase in voltage, and it is increasing and then slightly decreasing with the increase in wire feed rate.
- For deposition of high aspect ratio structure by using GMAW-WAAM, wire feed rate followed by the voltage are the most important parameters to be controlled.
- Laser marking before deposition shows a promising result, decreasing width by 33.5% and increasing aspect ratio by 50.3%, hence laser hybrid WAAM can be used to produce thin sections.

- The SEM analysis revealed an **increase in grain size** from 9.04 µm in the as-deposited sample to 12.81 µm after annealing.

- The XRD analysis indicates that certain peaks corresponding to the **Ti2Ni phase disappeared after annealing**, suggesting an increased formation of the NiTi phase.

- The DSC analysis shows a **reduction in average transformation temperature** and an increased austenitic transformation window for the annealed sample, with the Austenite Start (As) temperature at 34.61°C and the Austenite Finish (Af) temperature at 82.49°C.

- Micro-hardness testing revealed a **reduction in hardness**, decreasing from 337.3 Hv in the as-deposited sample to 302.54 Hv after annealing.

- The tensile test indicated an increase of ultimate tensile strength (UTS) from **199.13 MPa to 286.53 MPa** in the austenite phase and from **237.53 MPa to 404.8 MPa** in the martensite phase.
- EDS result depicts a **decrease in concentration of Ti** as we move in the direction of top layer from bottom layer across the cross section.
- The simulation results for the clamp and the fixture show that the clamp can take up to **40 N load** in its martensite state and the **fixture** is safe for training.
- EDS results for 9 samples deposited using full factorial design show that there is a **decrease in Ni atomic% with an increase in energy density.**
- DSC results show that there is an **increase in transformation temperature with the decrease in Ni concentration.**
- Solutionizing followed by aging shows a **increase in transformation temperature.**
- The **Cu inclusion increases the transformation temperature,** but the change is highly dependent on the percentage of Cu added.

Design of experiments and ANOVA was used to study the WAAM process parameters and then laser-hybrid WAAM was also studied. After understanding the WAAM process thoroughly, deposition of NiTi through WAAM was done using a full factorial design of experiments by varying voltage and wire-feed rate. The optimized deposition was selected based on the uniformity of deposition and least energy per unit length. Heat-treatment of optimized deposition was done, which significantly enhanced NiTi's microstructural and mechanical performance.

Also, the inclusion of Cu resulted in a change of transformation temperature. The optimized deposition was cut into a sheet and trained for actuation. 96.7% shape recovery was achieved on training. Future work will be on making a system for producing parts of specific transformation temperatures.

5.2 Future scope

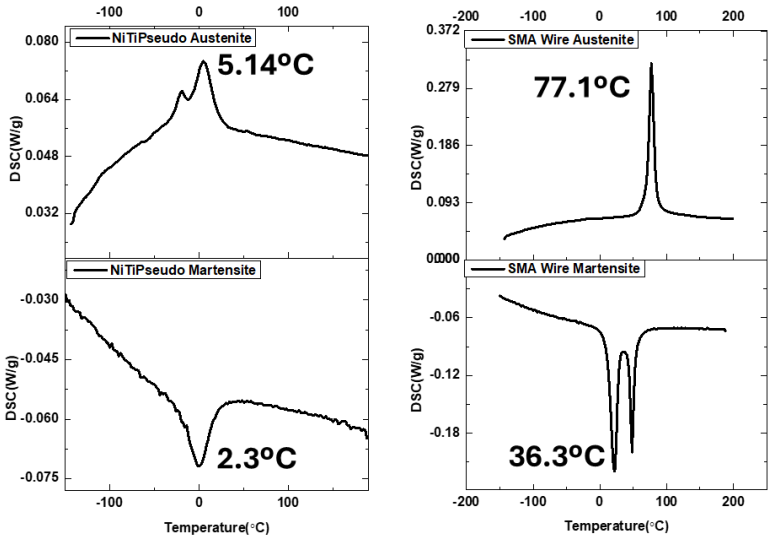

Fig. 5.1 Comparison of transformation temperature of SMA wire and Pseudoelastic wire.

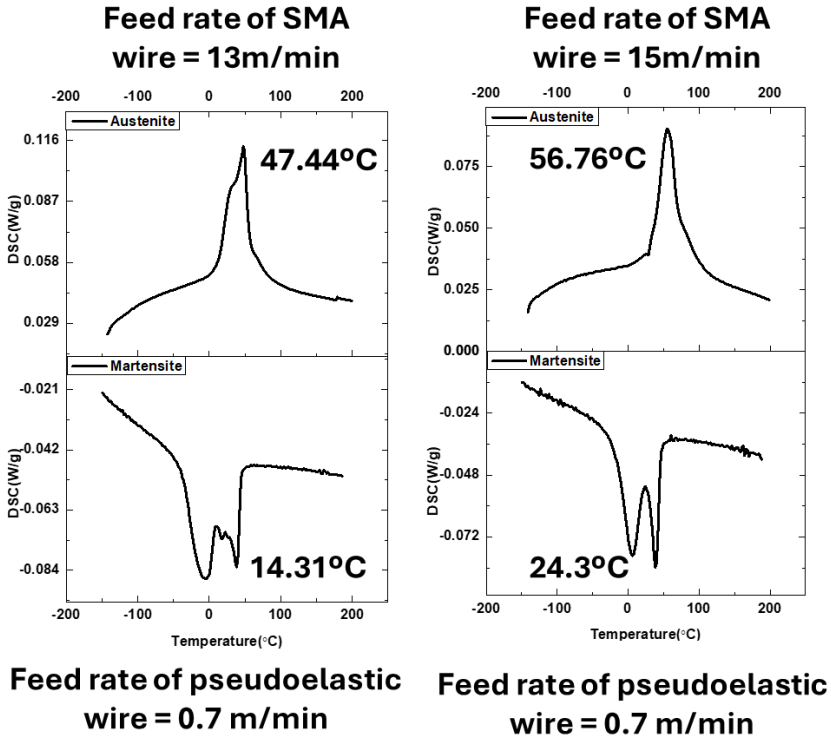

Fig. 5.2 Comparison of transformation temperature of (SMA+Pseudoelastic) depositions

The incorporation of shape-memory alloy (SMA) wire with pseudoelastic wire demonstrated that varying the feed rates of different wires during deposition leads to a distinct shift in transformation temperatures. This behavior highlights the potential for localized tuning of phase transformation characteristics through controlled material input. Future work should focus on developing a systematic framework or design methodology that enables the fabrication of components with spatially tailored transformation temperatures, thereby broadening the functional scope of SMA-based smart structures.

REFERENCES

[1] E. Farber, J. N. Zhu, A. Popovich, and V. Popovich, “A review of NiTi shape memory alloy as a smart material produced by additive manufacturing,” in *Materials Today: Proceedings*, Elsevier Ltd, 2019, pp. 761–767. doi: 10.1016/j.matpr.2020.01.563.

[2] R. Srivastava, S. H. Alsamhi, N. Murray, and D. Devine, “Shape Memory Alloy-Based Wearables: A Review, and Conceptual Frameworks on HCI and HRI in Industry 4.0,” *Sensors*, vol. 22, no. 18, Sep. 2022, doi: 10.3390/s22186802.

[3] A. Mohammadgholipour and A. M. Billah, “Mechanical properties and constitutive models of shape memory alloy for structural engineering: A review,” Dec. 01, 2023, *SAGE Publications Ltd*. doi: 10.1177/1045389X231185458.

[4] S. Miyazaki, K. Otsuka, and C. M. Wayman, “The shape memory mechanism associated with the martensitic transformation in Ti□Ni alloys—I. Self-accommodation,” *Acta Metallurgica*, vol. 37, no. 7, pp. 1873–1884, Jul. 1989, doi: 10.1016/0001-6160(89)90072-2.

[5] M. Chaturvedi, E. Scutelnicu, C. C. Rusu, L. R. Mistodie, D. Mihailescu, and S. Arungalai Vendan, “Wire arc additive manufacturing: Review on recent findings and challenges in industrial applications and materials characterization,” Jun. 01, 2021, *MDPI AG*. doi: 10.3390/met11060939.

[6] B. Liu, C. Yao, J. Kang, R. Li, and P. Niu, “Laser-Directed Energy Deposition of Fe-Mn-Si-Based Shape Memory Alloy: Microstructure, Mechanical Properties, and Shape Memory Properties,” *Materials*, vol. 17, no. 1, Jan. 2024, doi: 10.3390/ma17010131.

[7] Z. X. Khoo, J. An, C. K. Chua, Y. F. Shen, C. N. Kuo, and Y. Liu, “Effect of heat treatment on repetitively scanned SLM NiTi shape memory alloy,” *Materials*, vol. 12, no. 1, Jan. 2019, doi: 10.3390/ma12010077.

[8] M. Rashid, S. Sabu, A. Kunjachan, M. Agilan, T. Anjilivelil, and J. Joseph, “‘Advances in wire-arc additive manufacturing of nickel-based superalloys: Heat sources, DfAM principles, material evaluation, process parameters, defect management, corrosion evaluation and post-processing techniques,’” Nov. 01, 2024, *KeAi Publishing Communications Ltd.* doi: 10.1016/j.ijlmm.2024.05.009.

[9] D. T. Sarathchandra, M. J. Davidson, and G. Visvanathan, “Parameters effect on SS304 beads deposited by wire arc additive manufacturing,” *Materials and Manufacturing Processes*, vol. 35, no. 7, pp. 852–858, May 2020, doi: 10.1080/10426914.2020.1743852.

[10] A. Zavdoveev *et al.*, “Optimization of the pulsed arc welding parameters for wire arc additive manufacturing in austenitic steel applications,” *International Journal of*

Advanced Manufacturing Technology, vol. 119, no. 7–8, pp. 5175–5193, Apr. 2022, doi: 10.1007/s00170-022-08704-4.

[11] H. M. Vishwanatha *et al.*, "Effects of arc current and travel speed on the processing of stainless steel via wire arc additive manufacturing (WAAM) process," *J Adhes Sci Technol*, 2023, doi: 10.1080/01694243.2023.2289770.

[12] P. Badoniya, M. Srivastava, P. K. Jain, and S. Rathee, "Parametric investigation on wire arc additive manufacturing of ER70S-6 low-carbon steel for fabrication of thick-walled parts," *J Adhes Sci Technol*, 2023, doi: 10.1080/01694243.2023.2275823.

[13] V. T. Le *et al.*, "Prediction and optimization of processing parameters in wire and arc-based additively manufacturing of 316L stainless steel," *Journal of the Brazilian Society of Mechanical Sciences and Engineering*, vol. 44, no. 9, Sep. 2022, doi: 10.1007/s40430-022-03698-2.

[14] J. Vora *et al.*, "Fabrication of Multi-Walled Structure through Parametric Study of Bead Geometries of GMAW-Based WAAM Process of SS309L," *Materials*, vol. 16, no. 14, Jul. 2023, doi: 10.3390/ma16145147.

[15] M. R. Dehaghani, Y. Tang, S. Panicker, D. Wu, E. Coatanea, and G. G. Wang, "Modeling and optimization of height-related geometrical parameters for thin wall structures manufactured by metal additive manufacturing," *International Journal of Advanced Manufacturing Technology*, vol. 129, no. 9–10, pp. 4663–4675, Dec. 2023, doi: 10.1007/s00170-023-12618-0.

[16] R. Chaudhari, H. Parmar, J. Vora, and V. K. Patel, "Parametric Study and Investigations of Bead Geometries of GMAW-Based Wire–Arc Additive Manufacturing of 316L Stainless Steels," *Metals (Basel)*, vol. 12, no. 7, Jul. 2022, doi: 10.3390/met12071232.

[17] B. Ma, N. Zhang, Y. Zhang, and X. Gao, "Welding parameters effect and optimization on bead geometry during arc additive manufacturing," in *Journal of Physics: Conference Series*, IOP Publishing Ltd, Aug. 2021. doi: 10.1088/1742-6596/1986/1/012034.

[18] B. Liu *et al.*, "The Effects of Processing Parameters during the Wire Arc Additive Manufacturing of 308L Stainless Steel on the Formation of a Thin-Walled Structure," *Materials*, vol. 17, no. 6, Mar. 2024, doi: 10.3390/ma17061337.

[19] M. N, S. G, D. J, M. K. S, K. T, and V. R, "Significant Attention in Industry and Academia for Wire Arc Additive Manufacturing (WAAM) - A Review," *International Research Journal on Advanced Science Hub*, vol. 4, no. 07, pp. 198–204, Jul. 2022, doi: 10.47392/irjash.2022.048.

[20] A. Iturrioz, E. Ukar, and J. C. Pereira, “Influence of the manufacturing strategy on the microstructure and mechanical properties of Invar 36 alloy parts manufactured by CMT-WAAM,” *International Journal of Advanced Manufacturing Technology*, Jan. 2024, doi: 10.1007/s00170-024-14853-5.

[21] A. I. Albannai, H. León-Henao, and A. J. Ramirez, “Preventing columnar grains growth during hybrid wire arc additive manufacturing of austenitic stainless steel 316L,” *Engineering Reports*, Nov. 2024, doi: 10.1002/eng2.12914.

[22] Z. X. Khoo, Y. Liu, J. An, C. K. Chua, Y. F. Shen, and C. N. Kuo, “A review of selective laser melted NiTi shape memory alloy,” Mar. 29, 2018, *MDPI AG*. doi: 10.3390/ma11040519.

[23] S. K. Patel and A. Behera, “Evolution of Phases and their Influence on Shape Memory Effect by Varying Sintering Parameters of NiTi Alloys,” *Metals and Materials International*, vol. 28, no. 11, pp. 2691–2705, Nov. 2022, doi: 10.1007/s12540-021-01166-5.

[24] Y. Ba, Y. Lv, M. Yan, H. Jin, L. Guo, and Q. Zhang, “Effect of Energy Density on Mechanical Properties of NiTiCu Shape Memory Alloys Prepared by SLM,” *Materials*, vol. 17, no. 23, Dec. 2024, doi: 10.3390/ma17235693.

[25] F. Gantz, N. Al Jabri, D. Worrell, M. L. Young, and A. Palisoc, “Thermomechanical Processing of NiTiCu Shape Memory Alloy From Button to Wire,” in *ASME 2023 Conference on Smart Materials, Adaptive Structures and Intelligent Systems*, American Society of Mechanical Engineers, Sep. 2023. doi: 10.1115/SMASIS2023-111572.

[26] N. Sharma, K. K. Jangra, and T. Raj, “Fabrication of NiTi alloy: A review,” Mar. 01, 2018, *SAGE Publications Ltd*. doi: 10.1177/1464420715622494.

[27] T. C. da Silva *et al.*, “Microstructure, Thermal, and Mechanical Behavior of NiTi Shape Memory Alloy Obtained by Micro Wire and Arc Direct Energy Deposition,” *Journal of Manufacturing and Materials Processing*, vol. 9, no. 2, Feb. 2025, doi: 10.3390/jmmp9020057.

[28] A. Ramezannejad, D. East, A. B. Murphy, G. Lu, and K. V. Yang, “Optimising Additive Manufacturing of NiTi and NiMnGa Shape Memory Alloys: A Review,” *Metals (Basel)*, vol. 15, no. 5, p. 488, Apr. 2025, doi: 10.3390/met15050488.

[29] H. Dabbaghi, N. Taheri Andani, M. Pourshams, M. Sojoodi, B. Poorganji, and M. Elahinia, “Processability and Material Behavior of NiTi Shape Memory Alloys Using Wire Laser-Directed Energy Deposition (WL-DED),” *Journal of Manufacturing and Materials Processing*, vol. 9, no. 1, Jan. 2025, doi: 10.3390/jmmp9010015.

[30] L. Yu, K. Chen, Y. Zhang, J. Liu, L. Yang, and Y. Shi, “Microstructures and mechanical properties of NiTi shape memory alloys fabricated by wire arc additive manufacturing,” *J Alloys Compd*, vol. 892, Feb. 2022, doi: 10.1016/j.jallcom.2021.162193.

[31] A. Khismatullin, O. Panchenko, D. Kurushkin, I. Kladov, and A. Popovich, “Functional and Mechanical Properties of As-Deposited and Heat Treated WAAM-Built NiTi Shape-Memory Alloy,” *Metals (Basel)*, vol. 12, no. 6, Jun. 2022, doi: 10.3390/met12061044.

[32] W. C. Ke *et al.*, “Multi-layer deposition mechanism in ultra high-frequency pulsed wire arc additive manufacturing (WAAM) of NiTi shape memory alloys,” *Addit Manuf*, vol. 50, Feb. 2022, doi: 10.1016/j.addma.2021.102513.

[33] R. P. M. Guimarães *et al.*, “The electron beam freeform fabrication of NiTi shape memory alloys. Part II: Influence of the heat treatment on the superelastic behaviour,” *Proceedings of the Institution of Mechanical Engineers, Part L: Journal of Materials: Design and Applications*, vol. 238, no. 1, pp. 100–111, Jan. 2024, doi: 10.1177/14644207231184787.

[34] Y. Zhan, L. He, X. Lu, X. Zhu, and Q. Chen, “The Effect of Ageing Treatment on Shape-Setting and Shape Memory Effect of a NiTi SMA Corrugated Structure,” *Advances in Materials Science and Engineering*, vol. 2020, 2020, doi: 10.1155/2020/2846721.

[35] N. Sharma, A. Sharma, K. K. Goyal, S. Gupta, S. Bahl, and G. K. Sharma, “Transformation temperature and corrosion behavior of porous NiTi and NiTiCu shape memory alloy,” *Mater Today Proc*, vol. 63, pp. 215–218, Jan. 2022, doi: 10.1016/j.matpr.2022.02.519.

[36] S. Cai, J. E. Schaffer, T. Shi, J. Gao, and L. Kadeřávek, “Effect of Cu Alloying and Heat Treatment Parameters on NiTi Alloy Phase Stability and Constitutive Behavior,” *Shape Memory and Superelasticity*, Dec. 2024, doi: 10.1007/s40830-024-00504-x.

[37] Y. Cohen *et al.*, “Sinter-Based Additive Manufacturing of Ni-Ti Shape Memory Alloy,” May 2024, pp. 27–28. doi: 10.31399/asm.cp.smst2024p0027.

[38] A. Ramezannejad, D. East, A. B. Murphy, G. Lu, and K. V. Yang, “Optimising Additive Manufacturing of NiTi and NiMnGa Shape Memory Alloys: A Review,” *Metals (Basel)*, vol. 15, no. 5, p. 488, Apr. 2025, doi: 10.3390/met15050488.

[39] V. A. Yastrebov, M. Fischlschweiger, G. Cailletaud, and T. Antretter, “The role of phase interface energy in martensitic transformations: a lattice Monte-Carlo simulation,” Jan. 2014, doi: 10.1016/j.mechrescom.2013.11.006.

[40] *2018 International Symposium on Fundamentals of Electrical Engineering (ISFEE) : University Politehnica of Bucharest, Romania, November 1-3, 2018*. IEEE, 2018.

[41] V. A. Yastrebov, M. Fischlschweiger, G. Cailletaud, and T. Antretter, “The role of phase interface energy in martensitic transformations: a lattice Monte-Carlo simulation,” Jan. 2014, doi: 10.1016/j.mechrescom.2013.11.006.

[42] A. Tahaei, A. Aghajani, M. Abbasi, B. Bagheri, M. Merlin, and G. L. Garagnani, “Effects of Predefined Thermomechanical Procedure on the Microstructure and Mechanical Properties of the Two-Way Shape Memory Effect in the NiTi Alloy,” *Advances in Materials Science and Engineering*, vol. 2023, 2023, doi: 10.1155/2023/1524836.

[43] N. Agarwal *et al.*, “Effect of Heat Treatment Time and Temperature on the Microstructure and Shape Memory Properties of Nitinol Wires,” *Materials*, vol. 16, no. 19, Oct. 2023, doi: 10.3390/ma16196480.

[44] T. Assawakawintip, P. Santiwong, A. Khantachawana, K. Sipiyaruk, and R. Chintavalakorn, “The Effects of Temperature and Time of Heat Treatment on Thermo-Mechanical Properties of Custom-Made NiTi Orthodontic Closed Coil Springs,” *Materials*, vol. 15, no. 9, May 2022, doi: 10.3390/ma15093121.

[45] R. Bikbaev, N. Resnina, P. Anand Iyamperumal, S. Belyaev, and G. Thangamani, “Influence of thermocycling on the functional properties of the NiTi alloy produced by wire arc additive manufacturing,” Jun. 01, 2024, *Institute of Physics*. doi: 10.1088/2631-8695/ad4cb3.

[46] J. Vora *et al.*, “Optimization of Bead Morphology for GMAW-Based Wire-Arc Additive Manufacturing of 2.25 Cr-1.0 Mo Steel Using Metal-Cored Wires,” *Applied Sciences (Switzerland)*, vol. 12, no. 10, May 2022, doi: 10.3390/app12105060.